Nano Research

ISSN 1998-0124 CN 11-5974/O4
https://doi.org/10.1007/s12274-018-2268-5

Review Article

Review on photocatalytic and electrocatalytic artificial nitrogen fixation for ammonia synthesis at mild conditions: Advances, challenges and perspectives

Xiaolan Xue, Renpeng Chen, Changzeng Yan, Peiyang Zhao, Yi Hu, Wenjun Zhang, Songyuan Yang, and Zhong Jin (✉)

Key Laboratory of Mesoscopic Chemistry of MOE, School of Chemistry and Chemical Engineering, Nanjing University, Nanjing 210023, China

Received: 14 October 2018 / **Revised:** 2 December 2018 / **Accepted:** 12 December 2018

ABSTRACT

The ammonia synthesis from nitrogen and water under ambient conditions is one of the most inviting but challenging reaction routes. Although nitrogen is abundant in the atmosphere and the ammonia synthesis reaction is exothermic on the thermodynamics, the conversion of N_2 to ammonia is actually hard to proceed owing to the chemical inertness and stability of N_2 molecules. In industry, ammonia synthesis is carried out by the Haber-Bosch process under harsh conditions (300–500 °C, 20–30 MPa) associated with the requirement of substantial energy input and the enormous emission of greenhouse gases (e.g., CO_2). Recently, a growing number of studies on photo(electro)catalytic and electrocatalytic nitrogen reduction reaction (NRR) in aqueous solution have attracted extensive attention, which holds great promise for nitrogen fixation under room temperature and atmospheric pressure. However, the very low efficiency and ambiguous mechanism still remain as the major hurdles for the development of photochemical and electrochemical NRR systems. Here we provide an overview of the latest progresses, remaining challenges and future prospects in photocatalytic and electrocatalytic nitrogen fixation. Moreover, this review offers a helpful guidance for the reasonable design of photocatalysts and electrocatalysts towards NRR by combining theory predictions and experiment results. We hope this review can stimulate more research interests in the relatively understudied but highly promising research field of NRR.

KEYWORDS

heterogeneous catalysis, nitrogen fixation, ammonia synthesis, photocatalytic, electrocatalytic nitrogen reduction

1 Introduction

Nitrogen is an indispensable element to various bio-macromolecules vital to the course of life (such as proteins and nucleic acids) [1, 2]. The living organisms normally get nitrogen element in the forms of ammonia or nitrate instead of directly using the N_2 molecules, even though the content of N_2 is very high in atmosphere [3, 4]. This is because the nonpolar N≡N triple bond has a high bond energy of ~ 941 KJ·mol^{-1}, which is difficult for cleavage and hydrogenation [4–6]. At present, nitrogen fixation mainly proceeds in three approaches (Fig. 1): (a) biological nitrogen fixation by some azotobacteria that can fix N_2 molecules with nitrogenase [7]; (b) high energy nitrogen fixation in geochemical processes, such as lightning [3, 8]; (c) industrial nitrogen fixation through the energy-extensive Haber–Bosch method [9]. However, biological and geochemical nitrogen fixation only account for a small portion of the supply of fixed nitrogen. Haber–Bosch process is the major route for industrial ammonia synthesis by using N_2 and H_2 as sources and Fe-based materials as catalyst [10, 11]. This process requires substantial energy input and simultaneously generate huge emission of byproducts (for example, carbon dioxide) that may give rise to some undesirable global environmental changes [12, 13]. In consideration of the sustainable development of human society, it is highly desirable to develop eco-friendly and less energy-dependent strategies as substitutes for the Haber–Bosch process in the production of ammonia.

In nature, the nitrogenase enzymes in azotobacter can carry out the nitrogen fixation process at room temperature and atmospheric pressure [14, 15]. Inspired by the natural process, it is widely believed that photochemical and electrochemical reduction of nitrogen hold great potential for CO_2-emmision-free ammonia synthesis at ambient conditions, in which the nitrogen reduction reaction (NRR) is proceeded by the addition of protons and electrons ($N_2 + 6H^+ + 6e^- \rightarrow 2NH_3$) using solar power or renewable resource-derived electricity as driving force [16–18]. In these two methods, the N_2 molecules in air and the abundant H_2O are used as nitrogen source and proton source, respectively, and the nitrogen fixation can proceed at room temperature and atmospheric pressure. These advantageous features endow photochemical and electrochemical NRR with low energy consumption and CO_2 emission. By contrast, in the industrial ammonia synthesis process, the proton source is derived from H_2, with the necessity of high temperature and high pressure. These two approaches also have been regarded as the promising technologies for simultaneously alleviating the energy and environmental issues. However, although great research efforts have been dedicated to finding and designing suitable photocatalysts and electrocatalysts for ammonia synthesis, the yield of ammonia is still very low and these approaches are far from replacing the Haber–Bosch process. The insufficient efficiency of these heterogeneous NRR processes in aqueous solution is likely because of the weak adsorption and difficult activation of N_2 molecules on the surface of catalysts [19–21], the involvement of high-energy intermediates [20, 22, 23] and the complicated multi-electron transfer reaction

Address correspondence to zhongjin@nju.edu.cn

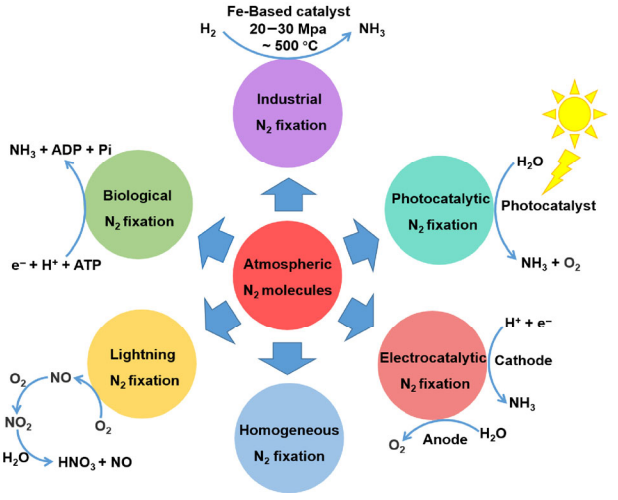

Figure 1 Schematic illustration of different reaction routes for nitrogen fixation.

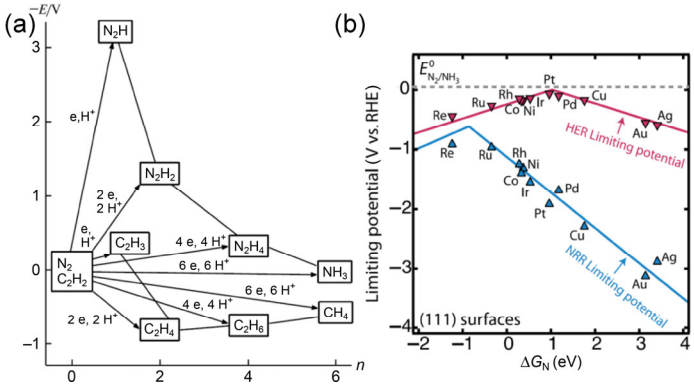

Figure 2 (a) The redox potentials (E) for one-, two-, four-, and six-electron transfer and hydrogenation on N_2 and C_2H_2 molecules, where n is the number of electrons. Reproduced with permission from Ref. [23], © Plenum Publishing Corporation 2003. (b) Volcano plot for NRR process on metals, with the corresponding plot of HER overlaid for comparison. Reproduced with permission from Ref. [37], © American Association for the Advancement of Science 2017.

pathway [19, 21]. In addition, the photocatalytic NRR process suffers from the weak reduction ability of photo-generated electrons and the recombination between photo-generated electrons and holes [24–26]. The efficiency of electrocatalytic NRR process is limited by the high over-potentials, low current densities, and low selectivity accompanied with the competition of hydrogen evolution reaction (HER) [27–29]. Therefore, the development of highly active and stable catalysts is vital to surmount the above issues. Herein, we present a review article that focuses on the following aspects: (i) the theoretical studies of heterogeneous NRR, (ii) the recent advances in photocatalytic nitrogen fixation, and (iii) the recent advances in electrocatalytic nitrogen fixation. Finally, this review provides a summary for discussing the major bottlenecks and giving future prospects in heterogeneous photocatalytic and electrocatalytic ammonia synthesis in aqueous solution.

2 Theoretical studies of heterogeneous nitrogen fixation in aqueous solution

Up to now, many researches have been conducted from the perspective of experiments and density functional theory (DFT) calculations to investigate the heterogeneous NRR mechanisms in aqueous solution. Analogous to the nitrogen fixation induced by nitrogenase enzyme complex, the overall process of heterogeneous nitrogen fixation in aqueous solution is widely considered as follows

$$N_2 + 6e^- + 6H^+ \rightarrow 2NH_3 \quad E^0 = -0.148 \text{ V vs. RHE} \qquad (1)$$

It has been proposed that the first step of the NRR process is based on the proton-coupled electron transfer (PCET) mechanism with the formation of N_2H^* species bounded on catalyst, according to Eq. (2). As shown in Fig. 2, the first electron transfer step requires very negative potential [23]. Subsequently, there are two possible intermediates, hydrazine (N_2H_4) and diazene (N_2H_2) that may participate in this protonation process, as shown in Eqs. (3) and (4) [22]. The desorption of NH_2^* species is possibly the last step. The corresponding equilibrium potentials are listed below

$$N_2 + e^- + H^+ \rightarrow N_2H \quad E^0 \approx -3.2 \text{ V vs. RHE} \qquad (2)$$

$$N_2 + 2e^- + 2H^+ \rightarrow N_2H_2 \quad E^0 \approx -1.1 \text{ V vs. RHE} \qquad (3)$$

$$N_2 + 4e^- + 4H^+ \rightarrow N_2H_4 \quad E^0 \approx -0.33 \text{ V vs. RHE} \qquad (4)$$

Therefore, the key barrier of NRR process in aqueous media could be ascribed to the generation of high energy intermediates.

In general, catalytic nitrogen fixation at a heterogeneous surface can be proceeded by two recognized mechanisms: associative mechanism and dissociative mechanism (Fig. 3) [30, 31]. In the

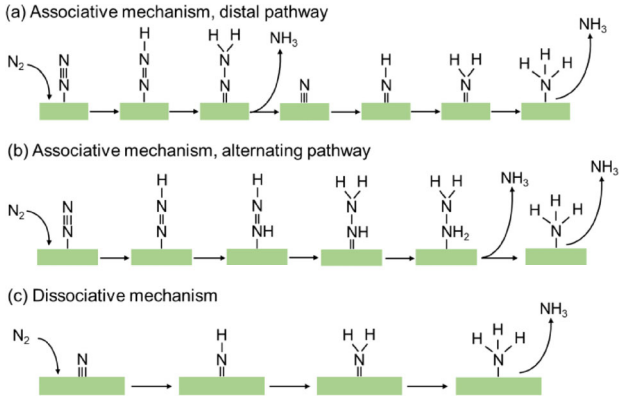

Figure 3 The possible reaction mechanisms of nitrogen fixation and ammonia synthesis on a heterogeneous surface. (a) and (b) The associative mechanism with the addition of protons proceeds by (a) the distal pathway and (b) the alternating pathway. (c) The dissociative mechanism.

associative mechanism, the nitrogen molecule is hydrogenated consecutively without breaking the N≡N triple bond until the first NH_3 molecule is released. It is believed that the hydrogenation in the associative mechanism proceeds through two possible pathways: the distal associative pathway and the alternating pathway. Protonation tends to take place on the nitrogen atom far away from the catalyst surface in the distal associative mechanism. However, in the alternating pathway, protons are in turn added onto the two nitrogen atoms of N_2 before one of the nitrogen atoms is converted into NH_3 by the N–N bond cleavage. In the dissociative mechanism, the addition of protons occurs after the N≡N triple bond is cleaved. It is generally accepted that N_2 molecules are hydrogenated by the associative mechanism in the biological nitrogen fixation process with nitrogenase [32, 33]. In contrast, the Haber-Bosch process is conducted by the dissociative mechanism, in which the N and H atoms react after the cleavage of N_2 triple bond and the H_2 bond [4]. However, DFT calculations indicate that the detailed pathways of heterogeneous catalytic NRR in aqueous solution vary from the catalytic systems and catalyst materials [17, 31]. At present, there are rare specific theoretical researches on photocatalytic nitrogen fixation [31]. On the contrary, theoretical studies on electrocatalytic ammonia production systems at ambient temperature and pressure are on the rise. Especially, DFT calculations are used to calculate the energy levels of possible pathways to determine the mechanisms and predict the promising catalysts for electrocatalytic NRR [34–36].

Skúlason et al. [34] presented a theoretical analysis of possible transition metal electrocatalysts for ammonia synthesis, in which

both the associative and dissociative Heyrovsky pathways on flat and stepped Ru (0001) surfaces were taken into consideration. In the associative mechanism, the rate-determining step is the addition of the first electron and proton onto $*N_2$ on the flat surface of Ru to produce the $*N_2H$ species. However, the formation of $*N_2H$ species is substantially more favorable on a stepped Ru surface. In the dissociative mechanism, the most difficult step is suggested to be the reduction of $*NH_2$ to NH_3 on the stepped Ru surface where the N_2 dissociation can only take place. To provide more theoretical guidance, the theoretical limiting potentials on different metal surfaces were linked to ΔE_N by a volcano plot obtained by DFT calculations, as shown in Fig. 2(b) [37]. This volcano plot is conducive to understand the rate-determining steps on different metal catalysts. On the metals that only bind N_2 weakly, the production of N_2H^* is the rate-determining step. In contrast, on the metals binding N_2 strongly, the reaction rates are limited by either the formation of NH_2^* (flat surfaces) or the production of NH_3 from NH_2^* (stepped surfaces). Moreover, it also indicates that some metals near the top of volcano plot for HER may exhibit a low Faradaic efficiency for ammonia synthesis owing to the competing reaction of HER. The dissociative mechanism of NRR process tends to occur on the flat surfaces of early transition metals (such as Sc, Y, Ti, and Zr), because N-adatoms normally bind more strongly than H-adatoms on the surfaces of these metals. In 2015, Nørskov et al. suggested that the electrochemical NRR process on metal surfaces under ambient conditions is likely to follow the associative mechanism, due to the considerable high kinetic barriers of N_2 dissociation [38]. Afterwards, an investigation about the energetics of all possible N–N dissociation steps for electrochemical N_2 reduction to ammonia on Ru stepped surface was conducted, revealing that the H-coverage can significantly affect the energy barriers for the first protonation of N_2 and the desorption of $*NH_2$ [39]. According to the calculated free energy diagrams, a thermodynamic limiting potential of −0.71 V is required for the dissociative pathways, which is comparable to that of the associative pathway (−0.68 V), indicating that all of possible reaction pathways in addition to the conventional associative and dissociative mechanisms should be taken into consideration.

Apart from metal catalysts, DFT calculations also predict that transition metal nitrides are promising electrocatalysts for N_2 reduction at low temperature and ambient pressure [35, 36, 40]. Besides, by calculating the N_2 adsorption energy, the reaction energies and the transition states in the reaction pathways using DFT method, Sun et al. claimed that two-dimensional M_3C_2 transition metal carbides (MXenes, such as V_3C_2 and Nb_3C_2) are promising candidates for electrocatalytic NRR [41]. In a word, the preferential mechanism and reaction pathway of heterogeneous NRR in aqueous solution strongly depend on the type of catalysts and the electron structure of active surfaces. Reasonable theoretical calculations combined with actual experimental results would be beneficial to better understand the detailed reaction process of NRR.

3 Advances in photocatalytic nitrogen fixation

The photocatalytic NRR process under ambient conditions has been extensively studied in experiments during the past few decades. Generally, there are two types of photo-conversion systems for NRR: photochemical cell system and photoelectrochemical cell system. The photochemical cell system utilizes semiconductor nanoparticle suspensions dispersed in N_2-saturated aqueous solutions as photocatalysts (Fig. 4(a)). In this system, both photo-reduction and photo-oxidation half-reactions occur on the different sites of the same semiconductor nanoparticles, which may result in the reverse reaction or re-oxidization of the desirable products. The photoelectrochemical cell system consists of photoelectrodes with different configurations, as shown in Fig. 4(b). The photoelectrodes harvest light to generate photo-induced electrons and holes and promote the charge separation. The NRR proceeds on the surface of photocathode, and the corresponding oxidation reaction occurs on the surface of counter electrode. It is suggested that the overall process of photo-driven NRR includes three essential steps in both photochemical and photoelectrochemical cell systems [42–44]. The first step of N_2 photo-reduction is photoexcitation, in which the photo-induced holes and electrons are generated in the valence band and conduction band of semiconductor nanoparticles, respectively. The second step includes the charge separation and migration of photo-induced carriers. Finally, the electrons diffuse across the bulk and the surface of semiconductor photocatalysts and reach the active sites, where the N_2 molecules adsorbed on the sites are reduced to ammonia by the electrons; at the same time, H_2O or other sacrificial reagents are oxidized by holes. However, the reduction of N_2 molecules needs a rather negative electrode potential position. As shown in Fig. 4(c), the reduction potential of solvated dinitrogen anions is −4.2 eV vs. normal hydrogen electrode (NHE) ($N_2 + e^- \rightarrow N_2^-$ −4.2 V vs. NHE) and another more accessible reduction potential is still up to −3.2 V vs. NHE ($N_2 + H^+ + e^- \rightarrow N_2H$ −3.2 V vs. NHE) [20]. Notably, the conduction band of most common semiconductors (such as TiO_2, g-C_3N_4, $SrTiO_3$, CdS and so on) can hardly reach such a negative position, resulting in the difficulty of solar driven nitrogen fixation. Therefore, the key issue

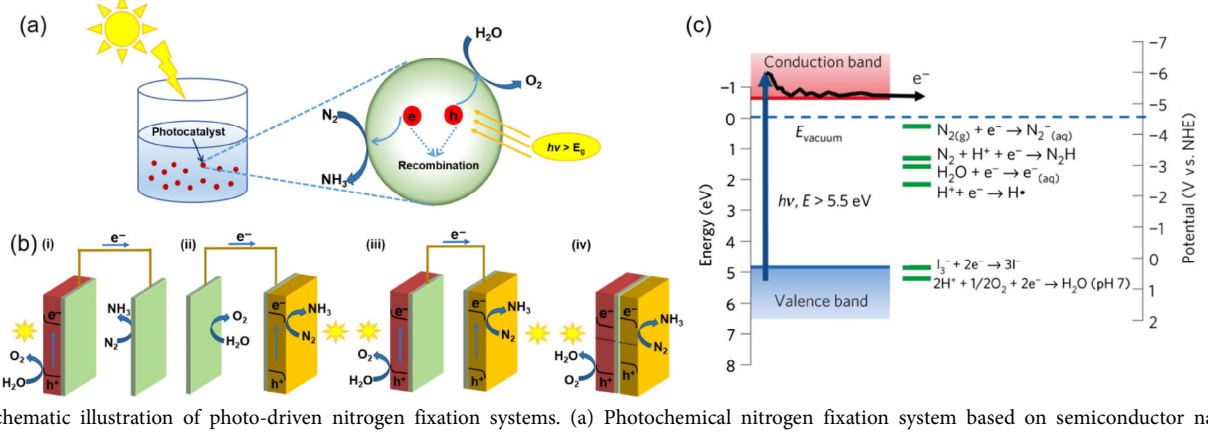

Figure 4 Schematic illustration of photo-driven nitrogen fixation systems. (a) Photochemical nitrogen fixation system based on semiconductor nanocatalysts dispersed in aqueous solution. (b) Photoelectrochemical nitrogen fixation system with photoelectrodes; (i) a photoanode coupled with a metal counter electrode; (ii) a photocathode with a metal counter electrode; (iii) a photoanode and a photocathode connected in a tandem configuration; (iv) a photoanode and a photocathode directly connected in a back-to-back configuration. (c) The valence band and conduction band of H-terminated diamond are compared with several relevant electrochemical reduction potentials. Reproduced with permission from Ref. [20], © Nature Publishing Group 2013.

of photo-driven NRR is to develop special semiconductor-based nanocatalysts with high efficiency and stability to produce ammonia under mild conditions. Numerous strategies including heteroatom doping, defects engineering, facet tailoring, and surface plasmon modification were employed to improve the photocatalytic efficiencies of the catalysts [45–49]. A performance summary of various catalysts for photochemical and photoelectrochemical NRR is presented in Table 1.

3.1 Photochemical nitrogen fixation

3.1.1 TiO_2 and other oxides based photocatalysts

As one of the earliest studied semiconductor photocatalysts, TiO_2-based photocatalysts has been investigated in nitrogen fixation very early, owing to its low cost, high stability and non-toxicity. In 1977, a pioneering research about the N_2 photo-reduction on TiO_2 was reported by Schrauzer and Guth [50]. They showed the chemisorbed N_2 on the powder mixtures of rutile and anatase TiO_2 with saturated H_2O vapor could be reduced to NH_3 under UV (ultraviolet) irradiation along with trace amounts of N_2H_4. They proposed that the rutile TiO_2 played a key role in nitrogen photo-fixation. Furthermore, iron doping could boost the yield of NH_3 and N_2H_4. The optimal Fe content was determined to be 0.2%, because Fe could accelerate the conversion of anatase TiO_2 to rutile TiO_2 under heat treatment but the active surface area of TiO_2 would be decreased when the iron content was above 0.2%. However, the effect of the defects induced by high temperature treatment which could play an important role in the N_2 photo-reduction was not taken into consideration.

In 1988, Bourgeois el al. reported that there was no NH_3 production on pristine anatase or rutile TiO_2 under UV irradiation, but the unmodified TiO_2 powders exhibited photocatalytic NRR activity after annealing at high temperature in air [51]. This result was attributed to the production of defects or impurity states in the bandgap of semiconductor and the surface hydroxyl groups after the high temperature treatment. Some other groups also prepared iron-doped TiO_2 by different routes and investigated the role of

Table 1 Summary of previously-reported catalysts for photochemical and photoelectrochemical NRR to NH_3 in aqueous solution under mild conditions

Catalyst	Conditions	Scavenger	Light source power (wavelength)	NH_3 yield ($\mu mol \cdot g_{cat.}^{-1} \cdot h^{-1}$)	Stability (retention of NH_3 yield)	Testing method	Reference
TiO_2 (rutile)	H_2O (g), 40 °C 1 atm	No	Hg-Arc Lamp 360 W (UV)	4.17	–	Kruse–Mellon colorimetric method	[50]
TiO_{2-x} (rutile)	40 °C 1 atm	2-Propanol	High-pressure Hg lamp 300 W (280–420 nm)	2.5	48 h	Ion chromatography Nessler's reagent	[55]
0.2 wt.% Fe-TiO_2	40 °C 1 atm	No	Hg-Arc Lamp 360 W (UV)	11.5	–	Kruse and Mellon colorimetric method	[50]
0.5 wt.% Fe-TiO_2	30 °C 1 atm	No	High-pressure Hg lamp 160 W (UV)	0.233 $\mu g \cdot m^{-2} \cdot h^{-1}$	–	Indophenol colorimetric method	[19]
Fe-doped TiO_2	25 °C	Ethanol	UV lamp 4 W (λ = 254 nm)	400	12 h	Nessler's reagent	[53]
2 wt.% Mg-TiO_2	–	No	Medium-pressure Hg lamp 400 W (UV)	10.35	2 h	Indophenol blue method	[57]
0.5 wt.% Cr-TiO_2	–	No	Osram HWL lamp 160 W	2.12 $\mu g \cdot m^{-2} \cdot h^{-1}$	–	Indophenol colorimetric method	[58]
10 wt.% V-TiO_2	–	No	Medium-pressure Hg lamp 400 W	6.12	–	Indophenol blue method	[59]
10 wt.% Ce-TiO_2	–	No	Medium-pressure Hg lamp 400 W	4.25	–	Indophenol blue method	[59]
5% $RuCl_3/TiO_2$	25 °C	Humic acid	Xe lamp 150 W	4 $\mu M \cdot cm^{-2} \cdot h^{-1}$	–	Kruse–Mellon colorimetric method	[60]
Au/TiO_2-OVs	30 °C 1 atm	Methanol	Xe lamp 300 W (λ > 420 nm)	78.6	9 h	Indophenol blue method	[56]
Fe, Ru or Os/TiO_2	25 °C	Ascorbic acid	Xe lamp 250 W	Ru (13.6) > Fe > Os	–	Indophenol blue method	[64]
Ru, Rh, Pd or Pt/TiO_2	–	Methanol	Xe lamp 150 W	Ru (29.4) > Rh > Pd > Pt	–	Indophenol colorimetric method	[65]
Pt/TiO_2	38 °C	No	High-pressure Hg lamp 100 W	9.3	–	Nessler's reagent	[96]
$Fe_2Ti_2O_7$ film	–	Ethanol	High-pressure Hg lamp (λ > 320 nm)	11.3	–	Kruse–Mellon colorimetric method	[61]
$Fe_2O_3 \cdot TiO_2$ $(H_2O)_n$	25 °C	No	Tungsten filament lamp 100 W	22 $\mu M \cdot h^{-1}$	–	Indophenol blue method	[71]
$Fe_2O_3(H_2O)_n$	26 °C	No pH = 10	Tungsten filament lamp 100 W	0.56	–	Indophenol blue method	[66]
Fe_2O_3	25 °C	Ethanol	Xe lamp 500 W	1365	4 h	Nessler's reagent	[67]
Reduced Fe_2O_3	29–30 °C	No	Xe lamp 150 W	10.0	580 h	Trichloramine method	[68]
$Fe_2O_3(H_2O)_n$/ bentonite	–	No	Medium-pressure Hg lamp 125 W	0.67	–	Indophenol blue method	[69]
P3MeT/TiO_2	20 °C	No	Xe lamp 100 W	17 $\mu mol \cdot m^{-2} \cdot h^{-1}$	–	Indo-naphthol method	[70]
$V_2O_3 \cdot Fe_2O_3 \cdot (H_2O)_n$	26 °C	No	Medium-pressure Hg lamp 400 W	8.33 $\mu M \cdot h^{-1}$	20 h	Indophenol blue method	[72]
$Sm_2O_3 \cdot nH_2O$ $V_2O_3 \cdot nH_2O$	26 °C	No	Medium-pressure Hg lamp 400 W	100 $\mu M \cdot h^{-1}$	–	Indophenol blue method	[73]
$Cu_2O \cdot nH_2O \cdot CuCl$	–	No	Medium-pressure Hg lamp 450 W	70.0 $\mu M \cdot h^{-1}$	–	Indophenol blue method	[74]

(Continued)

Catalyst	Conditions	Scavenger	Light source power (wavelength)	NH_3 yield ($\mu mol \cdot g_{cat.}^{-1} \cdot h^{-1}$)	Stability (retention of NH_3 yield)	Testing method	Reference
C-WO_3·H_2O	RT[a] AP[b]	No	Xe lamp 500 W	205	5 h (49%)	Nessler's reagent	[75]
Mo-$W_{18}O_{49}$ nanowires (1%)	RT[a] AP[b]	Na_2SO_3	Xe lamp 300 W	195.5	10 h	Ion chromatography Nessler's reagent	[76]
BiO quantum dots	25 °C AP[b]	No pH = 3.8	Xe lamp 500 W	1,226	120 h	Indophenol blue method	[77]
H-Bi_2MoO_6	–	No	300 W Xe lamp (λ > 400 nm)	1,300	13 h (~ 85%)	Nessler's reagent	[78]
BiOBr-001-OV	25 °C AP[b]	No	Xe lamp 300 W	223.3	–	Nessler's reagent	[81]
BiOBr-001-OV	25 °C AP[b]	No	Xe lamp 300 W (λ > 420 nm)	104.2	8 h (~ 85%)	Nessler's reagent	[81]
BiOCl	25 °C AP[b]	Methanol	Xe lamp 300 W	69.0	–	Nessler's reagent	[82]
Bi_5O_7Br ultrathin nanotubes	25 °C AP[b]	No	Xe lamp 300 W (λ > 400 nm)	1,380	10 h	Nessler's reagent	[83]
Bi_5O_7I-100	25 °C AP[b]	Methanol	Xe lamp 300 W	47.6 $\mu mol \cdot L^{-1} \cdot h^{-1}$	500 min (95%)	Nessler's reagent ^1H NMR	[84]
Bi_5O_7I-001	25 °C AP[b]	Methanol	Xe lamp 300 W	111.5 $\mu mol \cdot L^{-1} \cdot h^{-1}$	500 min (98%)	Nessler's reagent	[84]
V-g-C_3N_4	25 °C AP[b]	Methanol	Xe lamp 300 W (λ > 420 nm)	1,240	15 h	Nessler's reagent	[87]
Sponge-like g-C_3N_4	30 °C AP[b]	EDTA-2Na	High-pressure sodium lamp 250 W (400–800 nm)	166.7	4 h	Nessler's reagent	[88]
g-C_3N_4	30 °C AP[b]	Ethanol	High-pressure sodium lamp 250 W (400–800 nm)	83.6	4 h	Nessler's reagent	[89]
g-C_3N_4	30 °C AP[b]	Ethanol	High-pressure sodium lamp 250 W (400–800 nm)	175.5	20 h	Nessler's reagent	[90]
g-C_3N_4	30 °C AP[b]	Ethanol	High-pressure sodium lamp 250 W (400–800 nm)	141.7	20 h	Nessler's reagent	[91]
$Fe_{0.05}$-g-C_3N_4	30 °C AP[b]	Ethanol	High-pressure sodium lamp 250 W (400–800 nm)	300	4 h	Nessler's reagent	[92]
KOH treated g-C_3N_4	25 °C AP[b]	Methanol	Xe lamp 300 W	3,632	20 h	Nessler's reagent	[93]
m-PCN-V	30 °C AP[b]	No	Xe lamp 40.7 $W \cdot m^{-2}$ (420–600 nm)	1.0	24 h	Indophenol colorimetric method	[94]
TiO_2@C/g-C_3N_4	25 °C AP[b]	Methanol	Xe lamp 300 W (λ > 420 nm)	250.6	10 h	Nessler's reagent	[95]
Pt-CdS	38 °C	No	High-pressure Hg lamp 100 W	16.3	–	Nessler's reagent	[96]
$Ni_2P/Cd_{0.5}Zn_{0.5}S$	20 °C 1 atm	No	Xe lamp 300 W (λ > 400 nm)	254	4 h (92%)	Nessler's reagent	[97]
Ultrathin MoS_2	25 °C	No pH = 3.5	Xe lamp 500 W	65	10 h	Indophenol blue method	[98]
$Zn_{0.1}Sn_{0.1}Cd_{0.8}S$	30 °C AP[b]	Ethanol	High-pressure sodium lamp 250 W (400–800 nm)	263	4 h	Nessler's reagent	[99]
$Mo_{0.1}Ni_{0.1}Cd_{0.8}S$	30 °C AP[b]	Ethanol	High-pressure sodium lamp 250 W (400–800 nm)	178	4 h	Nessler's reagent	[100]
Fe(O)OH	26 °C	No	Medium-pressure Hg lamp 400 W	9.25 $\mu M \cdot h^{-1}$	24 h	Indophenol blue method	[101]
CuCr-LDH Nanosheets	25 °C	No	Xe lamp 300 W	73.9	–	Nessler's reagent	[102]
CuCr-LDH Nanosheets	25 °C	No	Xe lamp 300 W (λ > 400 nm)	57.1	5 h (~ 84%)	Nessler's reagent	[102]
$Bi_2O_2CO_3$ with defects	RT[a] AP[b]	Methanol	Xe lamp 500 W	398.8	20 h (92.15%)	Nessler's reagent	[103]
Boron-doped diamond	25 °C 1atm	KI	High-pressure Hg lamp 450 W (λ > 190 nm)	0.8 ppm after 24 h	–	Indophenol blue method	[20]
Au NPs/ Nb-$SrTiO_3$/Ru	RT[a]	Ethanol	Xe lamp 550–800 nm	1.1 $nmol \cdot cm^{-2} \cdot h^{-1}$	24 h	Salicylate–hypochlorite method	[106]
Au NPs/ Nb-$SrTiO_3$/Zr/ZrOx	RT[a]	No	Xe lamp 550–800 nm	0.73 $nmol \cdot cm^{-2} \cdot h^{-1}$	24 h	Salicylate–hypochlorite method	[107]
Au NPs/ Nb-$SrTiO_3$/Zr/ZrOx	RT[a]	Ethanol	Xe lamp 550–800 nm	6.5 $nmol \cdot cm^{-2} \cdot h^{-1}$	24 h	Salicylate–hypochlorite method	[107]
TiO_2/Au/a-TiO_2	–	No	Xe lamp 300 W	13.4 $nmol \cdot cm^{-2} \cdot h^{-1}$	12 h	Indophenol blue method	[108]
Au/black Si/Cr	–	Sulfite	Xe lamp 500 W	1.33 $\mu g \cdot cm^{-2} \cdot h^{-1}$	24 h	Ammonia/ammonium ISE Indophenol method	[109]

[a]RT denotes room temperature, [b]AP denotes atmosphere pressure.

iron. Radford and Francis prepared anatase and rutile TiO_2 doped with iron by metal vapor synthesis [52]. There was no ammonia formation on undoped samples. On the contrary, iron-doped anatase and rutile TiO_2 exhibited photocatalytic NRR activity and the former was much more active, which was different from Schrauzer's research. This result may be ascribed to the stronger driving force of anatase TiO_2 for NRR with more negative flat band potential. But it was unclear whether Fe directly participated in the photo-reduction process. Afterwards, Augugliaro et al. demonstrated that nitrogen photo-reduction took place only when the Fe^{3+} ions was in the TiO_2 matrix and the surface enrichment of Fe would decrease the activity [19]. This phenomenon was rationalized by the hypothesis that bulk Fe^{3+} ions could trap the electrons and thus inhibit the recombination of electrons and holes. Simultaneously, plenty of holes reached the surface of catalyst and reacted with hydroxyl groups to produce highly reactive OH· radicals, which could activate the inert N_2 molecules to form $[N_2$--OH]* complex. In 2014, Zhao et al. prepared Fe-doped TiO_2 nanoparticles with exposed (101) facets by a two-step hydrothermal method [53]. The TiO_2 with optimal Fe^{3+} doping displayed the highest quantum yield (18.27×10^{-2} m^{-2}) for NRR using ethanol as scavenger under 254 nm UV irradiation, which was 3.84 times higher than pristine TiO_2. The authors concluded that a small amount of Fe could trap photo-induced electrons and holes to inhibit the recombination of photo-generated carriers. Moreover, Fe-doping could facilitate the formation of oxygen vacancies (OVs), which was conducive to the adsorption of H_2O molecules and the production of surface –OH groups that could participate in the photocatalytic NRR process.

In 2002, Antonelli et al. reported the photo-reduction of N_2 to NH_3 using reduced mesoporous titanium oxide photocatalyst [54]. In this system, the ammonia synthesis was likely attributed to the cleavage of N≡N triple bonds by low-valence Ti centers followed by the reaction with water molecules. A recent report showed that noble-metal-free TiO_2 with abundant surface OVs could carry out artificial photosynthesis of NH_3 in pure water under UV light, and the highest solar-to-chemical energy conversion efficiency of 0.02% among the reported works was achieved [55]. The mechanism for the nitrogen fixation on the surface Ti^{3+} species of TiO_2 is shown in Fig. 5(a). It was proposed that the Ti^{3+} species on the OVs were the active sites for NRR. The N_2 molecules were firstly adsorbed on Ti^{3+} sites via the electron donation and then the N≡N bonds were activated, forming Ti^{4+}-azo species (Fig. 5(b) a → b). The interactions between the adsorbed N_2 molecules and the H atoms in nearby surface Ti-OH groups lead to the production of Ti^{4+}-azo' species (Fig. 5(b) b → c). Subsequently, the electrons in conduction band were trapped in the surface OVs and regenerated the Ti^{3+} sites, and then produce Ti^{4+}-hydrazo species associated with the water oxidation under light (Fig. 5(b) c → d → e). Finally, the NH_3 molecules were generated, accompanied by the re-formation of surface Ti^{3+} sites under irradiation (Fig. 5(b) e → f → a). Au nanocrystals anchored TiO_2 nanosheets with OVs (Au/TiO_2-OV) were used to reduce N_2 in a "working-in-tandem" pathway at ambient conditions (Figs. 5(c) and 5(d)) [56]. Firstly, the N_2 molecules were chemisorbed and activated by the OVs on TiO_2; secondly, the hot electrons

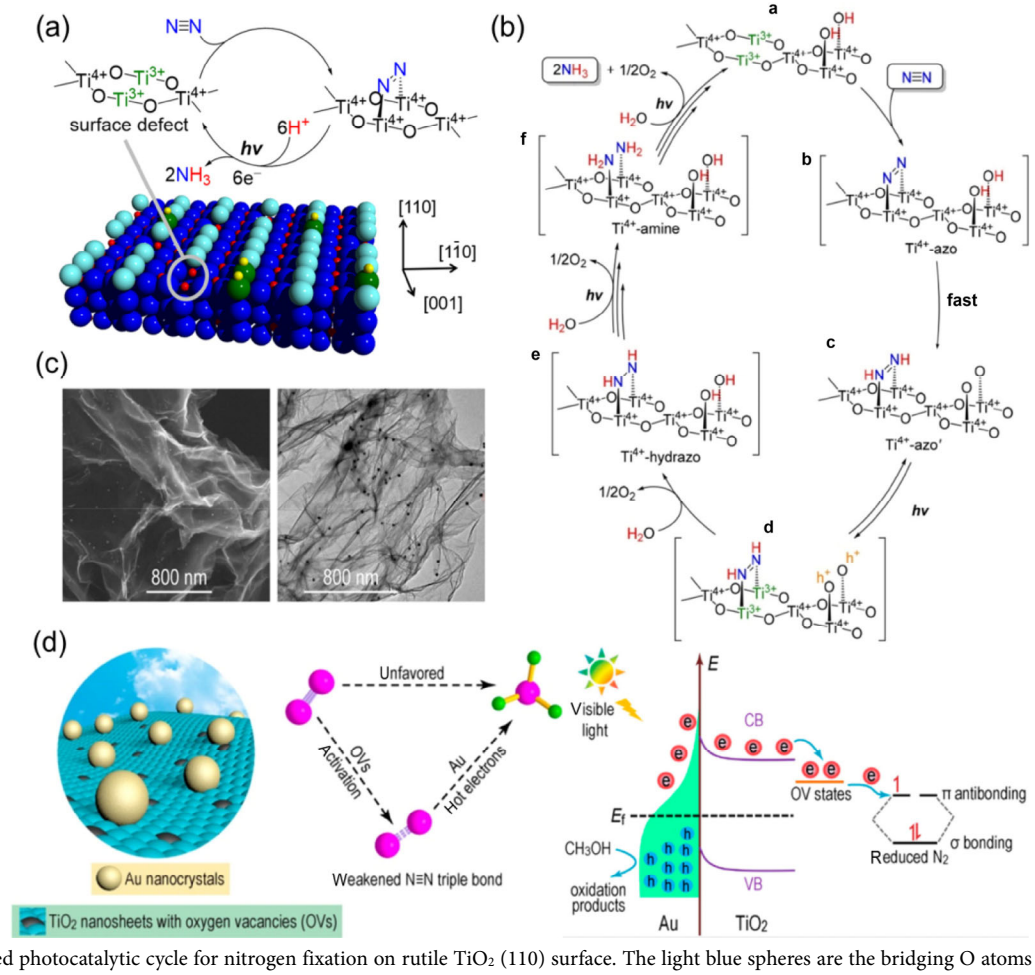

Figure 5 (a) Proposed photocatalytic cycle for nitrogen fixation on rutile TiO_2 (110) surface. The light blue spheres are the bridging O atoms (O_b) lying in the [001] azimuth; the red and blue spheres are the Ti and bulk O atoms, respectively; the green and yellow spheres are the O and H atoms in the surface–OH groups. (b) Proposed mechanism for photocatalytic NRR around the surface oxygen vacancies of TiO_2. Reproduced with permission from Ref. [55], © American Chemical Society 2017. (c) SEM and TEM images of Au/TiO_2-OV catalyst and (d) schematic of N_2 photo-reduction process on Au/TiO_2-OV catalyst induced by the synergistic effect between plasmonic Au and OV-rich TiO_2. Reproduced with permission from Ref. [56], © American Chemical Society 2018.

derived from the plasmonic Au nanocrystals diffused and were trapped by the OVs; finally, the OVs-activated N_2 molecules were reduced into NH_3 by the trapped hot electrons. A high apparent quantum efficiency of 0.82% at 550 nm was obtained by the Au/TiO_2-OV catalyst, indicating the improved performance for N_2 photo-fixation under visible light.

Many other metal species (such as Co, Mo, Ni, Pd, Mg, Cr, V, Ce, Ru, Fe and so on) also have been doped into TiO_2 in the early researches, but the photocatalytic activity was not satisfactory [50, 57–61]. Apart from serving as the dopants in TiO_2 matrix, the transition metal atoms loaded on TiO_2 can act as co-catalysts. Moreover, the formation of Schottky junctions between semiconductors and transition metal nanoparticles can create built-in electric fields on the interfaces and promote the separation of photo-induced electrons and holes [48, 62, 63]. Following this principle, noble metals were loaded on TiO_2 catalysts to improve the photocatalytic NRR performance. Rao and his partners showed the photocatalytic nitrogen fixation activity of metal loaded TiO_2 catalysts could be sorted as: Ru > Fe > Os [64]. Viswanathan et al. investigated the influences of noble metals loaded on TiO_2 and showed that the photocatalytic activity was in the order of: Ru > Rh > Pd > Pt, which is closely correlated with the strength of intermediary M–H bond and the overpotential for HER [65].

In addition to the above TiO_2-based photocatalysts, many other oxide-based photocatalysts were also investigated for N_2 photo-reduction. In 1987, Tennakone et al. reported that photo-driven NRR took place on amorphous hydrous ferric oxide under visible light. This photocatalytic activity was resulted from the negative flat band potential and strong chemisorption of N_2 on catalyst surface [66]. Lashgari and Zeinalkhani discovered that Fe_2O_3 nanoparticles synthesized by facile precipitation/calcination method could effectively fix N_2 to NH_3 [67]. Partially reduced Fe_2O_3 was also reported to be able to be used for photocatalytic NRR [68]. Ileperuma and coworkers loaded hydrous ferric oxide on montmorillonite clays and demonstrated that more NH_3 and less nitrates were produced on this catalyst compared to the pure hydrous ferric oxide under UV irradiation [69]. The improved photocatalytic activity was attributed to the larger surface area of hydrous ferric oxide loaded on montmorillonite clays and the retardation of ammonia photo-oxidation.

The inefficient charge separation and transfer to the solvent, the poor chemisorption of N_2 on catalyst surface and the back-reactions are the main obstacles to the photochemical NRR process. To overcome these problems, some feasible strategies have been developed to increase the specific NRR activity of photocatalysts, such as, by introducing defects or vacancies [55, 56], increasing the specific surface area of catalysts, or building hybrid material interfaces of composite catalysts or heterojunctions [45, 49]. Hoshino et al. developed a conducting polymer/TiO_2 heterojunction (P3MeT/TiO_2) with photocatalytic activity for NRR [70]. Tennakone et al. synthesized a photocatalyst of Ti (IV) and Fe (III) hydrous oxides with a Ti/Fe ratio of ~ 8%, in which hydrous TiO_2 served as hole accumulation centers and NRR proceeded at ferric oxide with highly negative flat band potential and strong N_2 chemisorption [71]. Vanadium (III)-substituted hydrous ferric oxide was prepared and exhibited improved photocatalytic NRR performance compared to pristine hydrous ferric oxide, owing to the vanadium (III) sites used as holes scavenger [72]. In 1993, the same group synthesized hydrous oxides of samarium (III) and vanadium (III) by co-precipitation method. The part of Sm_2O_3·nH_2O with sufficiently negative band position was used to reduce N_2 to ammonia, and the part of V_2O_3·nH_2O acted as the holes sacrificial agent [73]. Hydrous cuprous oxide was also reported to be able to convert N_2 to NH_3 under light irradiation, presumably attributed to favorable N_2 chemisorption, negative flat band potential and self-sacrifice of Cu_2O·xH_2O [74].

Recently, a relatively high N_2 reduction rate (205 μmol·$g_{cat.}^{-1}$·h^{-1}) was obtained on the carbon-WO_3·H_2O hybrids in pure water under simulated sunlight [75]. In this system, carbon played a significant role in activating N_2 molecules and facilitating the separation and transport of photo-induced carriers. Xiong and his co-workers reported a strategy for tuning the activation of inert N_2 molecules by refining the defect states of $W_{18}O_{49}$ ultrathin nanowires (UTNWs) by Mo doping (Figs. 6(a)–6(e)) [76]. The doped low-valence Mo species could generate Mo–W centers as the active sites for N_2 activation, at which the adsorbed N_2 molecules were more polarized for better activation. Furthermore, Mo doping enhanced the metal–oxygen covalency, promoted the electron transfer to N_2 molecules and elevated the defect band center toward the Fermi level, thus providing more energetic electrons for nitrogen fixation. Benefiting from the above advantages, the 1 mol% Mo-doped $W_{18}O_{49}$ (MWO-1) exhibited a NH_3 yield rate of 195.5 μmol·$g_{cat.}^{-1}$·h^{-1}, about 8 times that of pristine $W_{18}O_{49}$. The apparent quantum efficiency and solar-to-ammonia efficiency were up to 0.33% at 400 nm and 0.028% under simulated AM 1.5 G light, respectively.

Sun et al. reported that BiO quantum dots (Fig. 6(f)) could efficiently fix nitrogen with an ammonia generation rate of 1,226 μmol·$g_{cat.}^{-1}$·h^{-1} under simulated solar light in the absence of any sacrificial reagent or co-catalyst [77]. They demonstrated low valence state Bi (II) species were conducive to N_2 activation and hydrogenation by temperature programmed desorption experiments and DFT calculations. A possible reaction mechanism of this process is presented in Fig. 6(g). N_2 molecule donates electrons to the empty 6d orbitals of Bi atom and meanwhile the unoccupied anti-bonding orbitals (σ^*2p_x, p^*2p_y, and p^*2p_z) of N_2 molecule accept electrons from the lone pairs of Bi atoms, generating a $1N_2$–3Bi (II) side-on bond structure, which greatly weaken the N≡N bond and accelerate the subsequent photochemical NRR process. Hydrogenated bismuth molybdate nanoframe was used as a novel photocatalyst for ammonia synthesis from air and water molecules without any scavengers [78]. The efficient and stable photocatalytic performance of nitrogen fixation (1.3 mmol·$g_{cat.}^{-1}$·h^{-1}) was ascribed to the unsaturated Mo atoms in MoO_6 coordination polyhedrons acting as activation centers to adsorb and activate N_2 molecules.

3.1.2 *Oxyhalides based photocatalysts*

Bismuth oxyhalides (BiOX, X = Cl, Br, or I) have drawn broad attention as 2D layered semiconductor photocatalysts with tetragonal matlockite structure. The layered structures make up of $[Bi_2O_2]^{2+}$ slabs are separated by two slabs of halogen atoms by the van der Waals interaction, which is easy to generate vacancies beneficial to photocatalytic activities [79, 80]. In addition, BiOX with an indirect bandgap can effectively inhibit the recombination of photo-generated electrons and holes. In 2015, Zhang et al. demonstrated efficient nitrogen fixation on BiOBr nanosheets by introducing oxygen vacancies (OVs) into the exposed (001) facets [81]. As illustrated in Fig. 7(a), theoretical simulation indicates that N_2 can be activated by the OVs on BiOBr {001} facets. The length of N≡N triple bond of the adsorbed N_2 on OVs elongates to 1.133 Å, longer than the bond length of original N≡N (1.078 Å). The photocatalytic NRR rate on BiOBr nanosheets in ultrapure water without any sacrificial regent reached up to 104.2 μmol·$g_{cat.}^{-1}$·h^{-1} under visible light and 223.3 μmol·$g_{cat.}^{-1}$·h^{-1} under UV–visible light (Fig. 7(b)). It was suggested that the electrons trapped by the OVs could jump into the empty antibonding orbitals of activated N_2 molecules and then reduce N_2 to ammonia (Fig. 7(c)). To get deeper understanding of the role of OVs, the mechanism of nitrogen fixation on the OVs of different exposed facets of BiOCl was investigated [82]. Figure 7(d) shows the determined energy level diagrams of the NRR process on {001} and {010} facets of BiOCl nanosheets, indicating that the

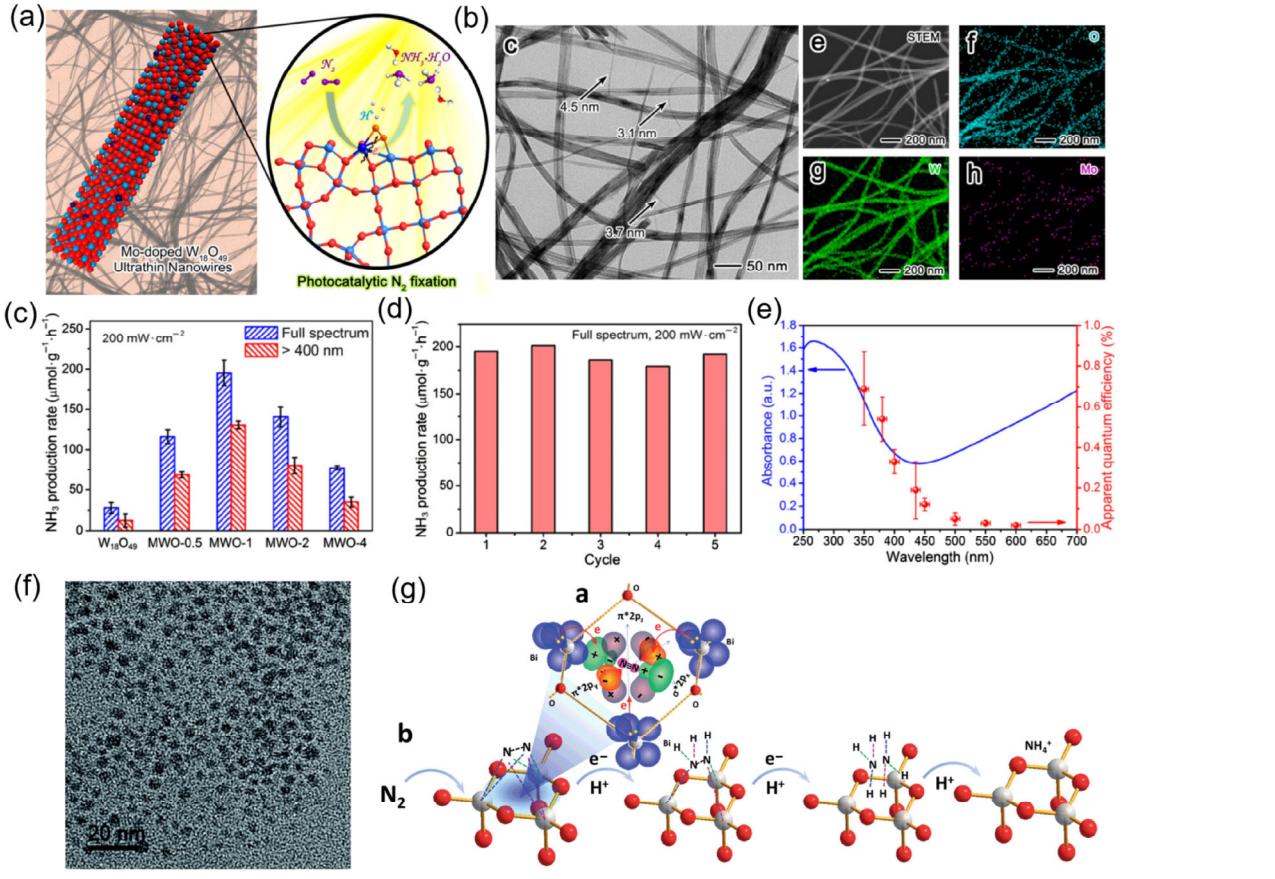

Figure 6 (a) Schematic illustration of photocatalytic NRR process on Mo-doped $W_{18}O_{49}$ UTNWs. (b) TEM, STEM and corresponding EDX elemental mapping images of MWO-1. (c) Photocatalytic ammonia generation rates of $W_{18}O_{49}$, MWO-0.5, MWO-1, MWO-2, and MWO-4 UTNWs under full-spectrum or visible–NIR light (λ > 400 nm) of 200 mW·cm^{-2} with Na_2SO_3 as sacrificial agent. (d) Photocatalytic ammonia generation rates in the first 2 h of cyclic test of MWO-1 UTNWs. (e) The apparent quantum efficiencies of photocatalytic NRR over MWO-1 UTNWs in pure water under monochromatic light irradiation. Reproduced with permission from Ref. [76], © American Chemical Society 2018. (f) TEM image of BiO quantum dots. (g) N_2 activation and reduction process on BiO catalyst. Reproduced with permission from Ref. [77], © Royal Society of Chemistry 2017.

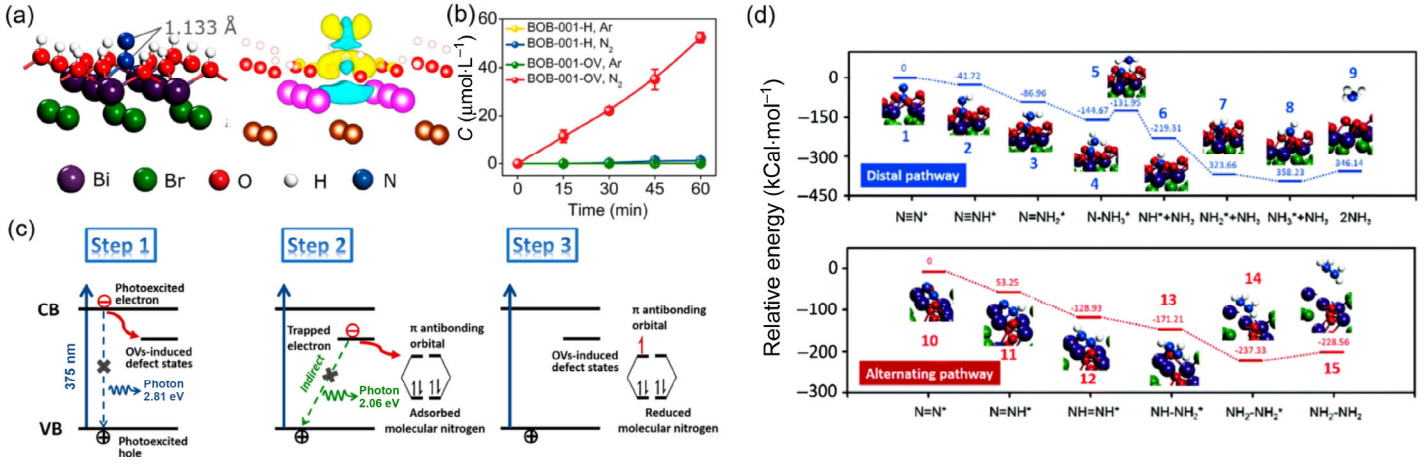

Figure 7 (a) (left) N_2 adsorption geometry on the OV of BiOBr (001) surface. (right) Charge density difference of N_2-adsorbed (001) surface. The yellow and blue isosurfaces represent charge accumulation and depletion in the space, respectively. (b) Generation rates of NH_3 under visible light (λ > 420 nm). (c) Schematic enhanced interfacial electron transfer processes induced by OVs. Reproduced with permission from Ref. [81], © American Chemical Society 2015. (d) Free energy change against the reaction coordinate. Reproduced with permission from Ref. [82], © Royal Society of Chemistry 2016.

hydrogenation of end-on adsorbed N_2 on the OVs of BiOCl {001} facets follows the associative distal pathway, while the nitrogen fixation on the OVs of BiOCl {010} facets occurs preferentially via the associative alternating pathway.

However, the introduced surficial oxygen vacancies on BiOX could be easily oxidized during the reaction, resulting in the rapid decline of photocatalytic NRR activity. To alleviate this issue, ultrafine Bi_5O_7Br nanotubes with abundant and sustainable oxygen vacancies were used to boost solar-driven ammonia synthesis in water without any sacrificial reagents or co-catalysts (Fig. 8) [83]. The Bi_5O_7Br nanotubes showed a high ammonia generation rate of 1.38 mmol·$g_{cat.}^{-1}$·h^{-1}, with an apparent quantum efficiency of ~ 2.3% at 420 nm, as presented in Fig. 8(b). Besides, bismuth-rich Bi_5O_7I nanosheets with dominant exposed {001} and {100} facets were employed in photocatalytic NRR [84]. Bi_5O_7I-001 exhibits a higher photocatalytic NH_3 production rate of 111.5 μmol·L^{-1}·h^{-1} compared to

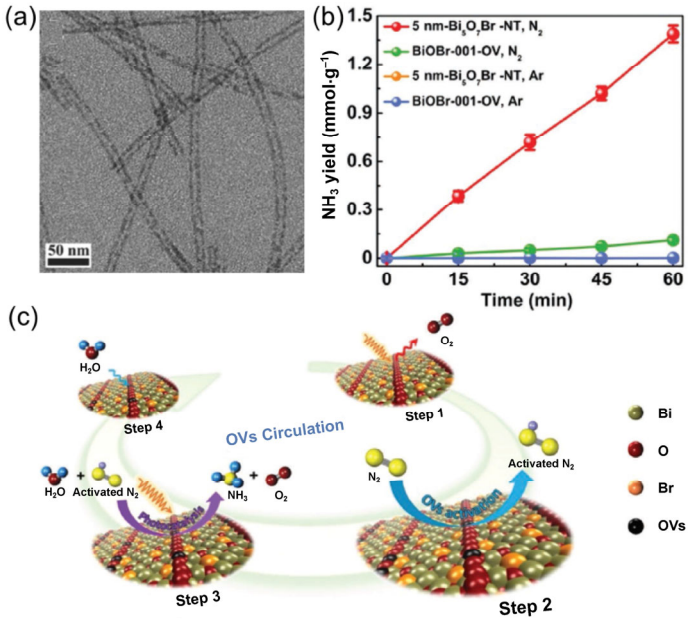

Figure 8 (a) TEM image of ultrafine Bi_5O_7Br nanotubes. (b) Ammonia yields of ultrafine Bi_5O_7Br nanotubes and BiOBr-001-OV nanosheets under visible light (λ > 400 nm) irradiation in pure water. (c) Schematic illustration of the photocatalytic NRR process on Bi_5O_7Br nanotubes. Reproduced with permission from Ref. [83], © Wiley-VCH 2017.

Bi_5O_7I-100 (47.6 μmol·L^{-1}·h^{-1}), owing to the more negative conduction band position of Bi_5O_7I-001 with a stronger reduction ability, while the in-depth mechanism still needs to be explored.

3.1.3 *Graphitic nitride carbon (g-C_3N_4) based photocatalysts*

As a two-dimensional conjugated polymer, graphitic carbon nitride (g-C_3N_4) has received considerable attention as a low-cost and stable photocatalyst with visible light response for solar energy conversion applications, including photocatalytic water splitting, CO_2 reduction, organic synthesis, environmental purification, and so on [85, 86]. Herein, the recent advances in g-C_3N_4 photocatalysts for photocatalytic NRR are summarized.

In 2015, Dong et al. demonstrated that the photocatalytic nitrogen fixation activity of g-C_3N_4 could be dramatically improved by introducing nitrogen vacancies (NVs) [87]. This is mainly because the NVs with the same shape and size as the nitrogen atoms are beneficial to adsorb and activate the chemically inert N_2. Moreover, NVs served as the traps of photo-excited electrons can facilitate the separation of electrons and holes. The photocatalytic ammonia generation rate was 1.24 mmol·$mg_{cat.}^{-1}$·h^{-1} in 20% methanol aqueous solution under visible light. Loading of Pd nanoparticles onto V-g-C_3N_4 can completely inhibit photocatalytic NRR, confirming the significant role of NVs of g-C_3N_4 for NRR. Afterwards, different kinds of g-C_3N_4 based photocatalysts were employed in photochemical ammonia synthesis [88–95].

Notably, honeycombed g-C_3N_4 doped with Fe^{3+} showed improved performance for photocatalytic NRR [92]. Experimental and theoretical calculation results demonstrated that Fe^{3+} sites were conducive to the chemisorption and activation of inert N_2 molecules. In addition, Fe^{3+} doping can control the morphology of g-C_3N_4 and facilitate interfacial electron transfer. Phosphorus-doped carbon nitride with surface NVs (PCN-V) was used to reduce N_2 under visible light, where the doped P atoms contributed to water oxidation and the nitrogen vacancies promoted N_2 reduction [94]. MXenes derived TiO_2@C/g-C_3N_4 heterojunctions with abundant surface defects, good light absorption and charge transport properties were synthesized, exhibiting a high NH_3 production rate of 250.6 μmol·$g_{cat.}^{-1}$·h^{-1} under visible light irradiation [95].

3.1.4 *Transition-metal sulfides and other photocatalysts*

Transition-metal sulfides have attracted extensive research interest as photocatalysts with relatively narrow bandgaps. Back in 1980, CdS was reported to be able to fix N_2 molecules, although the ammonia yield was very low [96]. Unfortunately, there were few breakthrough results on N_2 photo-reduction of sulfides due to the severe photo-corrosion. In 2017, $Cd_{0.5}Zn_{0.5}S$ solid solution was used to photochemically reduce N_2 [97]. When loaded with Ni_2P, $Cd_{0.5}Zn_{0.5}S$ showed an ammonia production rate of 253.8 μmol·$g_{cat.}^{-1}$·h^{-1} in deionized water under visible light with a quantum efficiency of 4.32% at 420 nm. It was suggested that Ni_2P as a co-catalyst greatly promoted the transfer of photo-induced electrons and holes. Wang et al. presented that photochemical NRR could proceed on ultrathin MoS_2 nanosheets with an ammonia synthesis rate of 325 μmol·$g_{cat.}^{-1}$·h^{-1} in deionized water (pH = 3.5), while bulk MoS_2 had no activity of ammonia synthesis [98]. This is because the ultrathin MoS_2 nanosheets can generate light-induced trions with high concentration of localized electrons, which is favor of the multi-electron process of N_2 photo-fixation. Inspired by the successful NRR process on photocatalysts with OVs and NVs, Hu and his partners demonstrated that $Zn_{0.1}Sn_{0.1}Cd_{0.8}S$ and $Mo_{0.1}Ni_{0.1}Cd_{0.8}S$ with sulfur vacancies could also promote the photo-conversion of N_2 to NH_3 under visible light, because sulfur vacancies used as electrons traps effectively prevented the recombination of photo-induced electrons and holes [99, 100].

In addition to the above photocatalysts, FeOOH was also proved to be capable of N_2 photo-conversion in 1991 [101]. Recently, Zhang et al. reported that layered double hydroxide (LDH) nanosheets can be used for nitrogen fixation in visible light region, as displayed in Fig. 9 [102]. Specially, CuCr-LDH ultrathin nanosheets displayed the optimal photocatalytic ammonia production rate under visible light in water without any sacrificial reagent. This result was ascribed to the distorted structure and compressive strain of ultrathin LDH nanosheets arising from the abundant oxygen defects, which greatly facilitated N_2 chemisorption and activation.

The presence of surface vacancies on nanomaterials can modify the electronic structure and reduce the coordination number of surface atoms, contributing to the formation of dangling bonds and enhancing catalytic performance. Therefore, reasonable vacancy engineering on nanocatalysts is feasible for improving NRR performance. Very recently, bismuth subcarbonate ($Bi_2O_2CO_3$) with controllable defect density was employed for photocatalytic NRR,

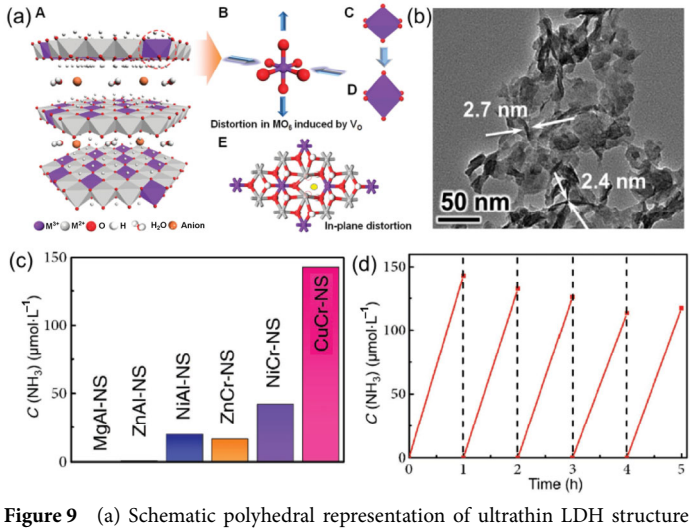

Figure 9 (a) Schematic polyhedral representation of ultrathin LDH structure with defective MO_6 octahedra at the edge and surface of LDH nanosheets. (b) TEM image of CuCr-LDH nanosheets. (c) Ammonia yields over a 1 h test period of different LDH photocatalysts (λ > 400 nm). (d) NRR cycling tests of CuCr-LDH nanosheets under visible light in water. Reproduced with permission from Ref. [102], © Wiley-VCH 2017.

revealing that the presence of surface vacancies significantly improved its photocatalytic performance [103].

3.2 Photoelectrochemical nitrogen fixation

The photocatalytic system using semiconductor nanocatalysts suspended in aqueous solution suffers from some drawbacks, such as the rapid recombination of photo-generated electrons and holes, the occurrence of undesirable side reactions, and the complex post-separation. Photoelectrochemical cells are another class of promising setups for solar-driven nitrogen fixation [104, 105]. Hamers and his teammates reported that solvated electrons generated on diamond by UV illumination could drive the kinetically-inert NRR process [20]. The ammonia yields in dual-compartment H-cell are higher than that in single-compartment cell (Fig. 10). In this system, B-doped diamond ejected electrons into solution to generate solvated electrons capable of directly participated in high-energy NRR process, which was free from the drawback of weak N_2 adsorption on catalyst surface.

A plasmon-induced photoelectrochemical NRR process under visible light was achieved on strontium titanate ($SrTiO_3$) photoelectrode loaded with gold nanoparticles [106]. The difference in pH between anodic chamber and cathodic chamber provided a chemical bias and ethanol as hole acceptor was added to the anodic compartment. The plasmon-induced charge separation at the Au/$SrTiO_3$ interface facilitated the oxidation in anodic chamber and the nitrogen reduction on Ru in the cathodic chamber. However, this system exhibited very low NRR activity and required sacrificial agents. Based on this work, the same group developed a new $SrTiO_3$ based photoelectrode by depositing a zirconium/zirconium oxide (Zr/ZrO_x) thin film on one side and loading Au nanoparticles on the opposite side, as shown in Fig. 11(a) [107]. The ammonia yield rate was 0.73 $nmol \cdot cm^{-2} \cdot h^{-1}$ without any sacrificial reagent. When ethanol was used as electron donor, the Au-NPs/Nb-$SrTiO_3$/Zr/ZrO_x photoelectrode exhibited high selectivity for NH_3 production and a higher ammonia generation rate of 6.5 $nmol \cdot cm^{-2} \cdot h^{-1}$ compared to Au-NPs/Nb-$SrTiO_3$/Ru photoelectrode (1.1 $nmol \cdot cm^{-2} \cdot h^{-1}$) (Fig. 11(b)). The high selectivity for ammonia production on Au-NPs/Nb-$SrTiO_3$/Zr/ZrO_x was mainly attributed to the smaller adsorption energy of N (ΔN^*) than H (ΔH^*) on the Zr surface. Very recently, Gong et al. introduced OVs onto the surface of rutile TiO_2 photoelectrodes by atomic layer deposition (ALD) (Fig. 11(c)) [108]. They demonstrated the synergistic effect of surface OVs and plasmonic Au nanoparticles on TiO_2/Au/a-TiO_2 photoelectrode for enhancing the photocatalytic NRR performance, as shown in Figs. 11(d) and 11(e).

Ali and coworkers prepared a nanostructured photoelectrode based on plasmon-enhanced black silicon for solar-driven nitrogen fixation [109], as shown in Figs. 12(a) and 12(b). Photochemical ammonia synthesis occurred in the reaction cell under 300 W Xe

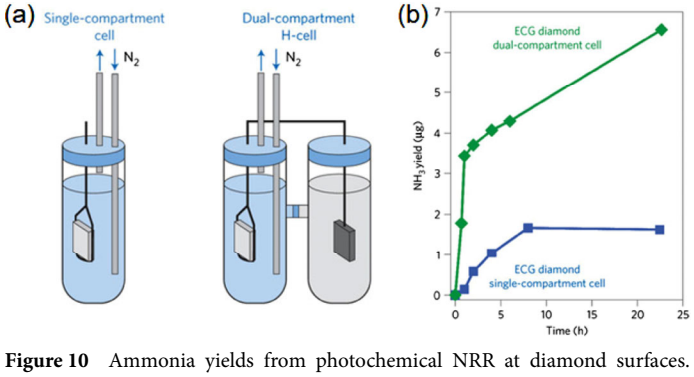

Figure 10 Ammonia yields from photochemical NRR at diamond surfaces. (a) Schematic diagram of reaction vessels with (left) single-compartment cell and (right) dual-compartment H-cell. (b) Total ammonia yields from ECG diamond in N_2-saturated water using single-compartment and dual-compartment H-cell. Reproduced with permission from Ref. [20], © Nature Publishing Group 2013.

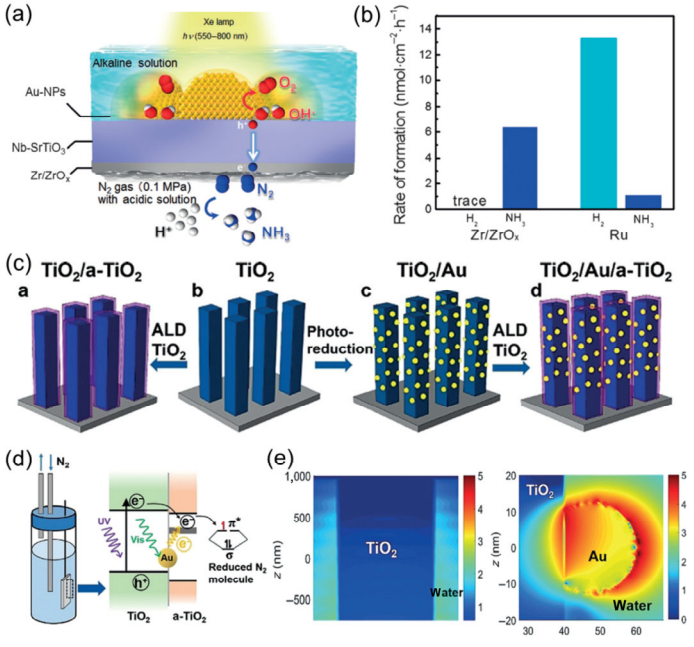

Figure 11 (a) Diagrammatic sketch of NH_3 photosynthesis on Au-NPs/Nb-$SrTiO_3$/Zr/ZrO_x photoelectrode. (b) Product selectivity comparison of Au-NPs/Nb-$SrTiO_3$/Zr/ZrO_x and Au-NPs/Nb-$SrTiO_3$/Ru photocathodes with ethanol as sacrificial electron donor. Reprinted with permission from Ref. [107], © Wiley-VCH 2016. (c) Preparation process of bare TiO_2, TiO_2/Au, TiO_2/a-TiO_2 and TiO_2/Au/a-TiO_2 photoelectrodes. (d) Schematic illustration of the synergistic effect of surface OVs and plasmonic Au NPs on TiO_2/Au/a-TiO_2 for N_2 photo-fixation. (e) FDTD simulations of electric field enhancement over TiO_2 and TiO_2/Au catalysts at 544 nm. Reproduced with permission from Ref. [108], © Wiley-VCH 2018.

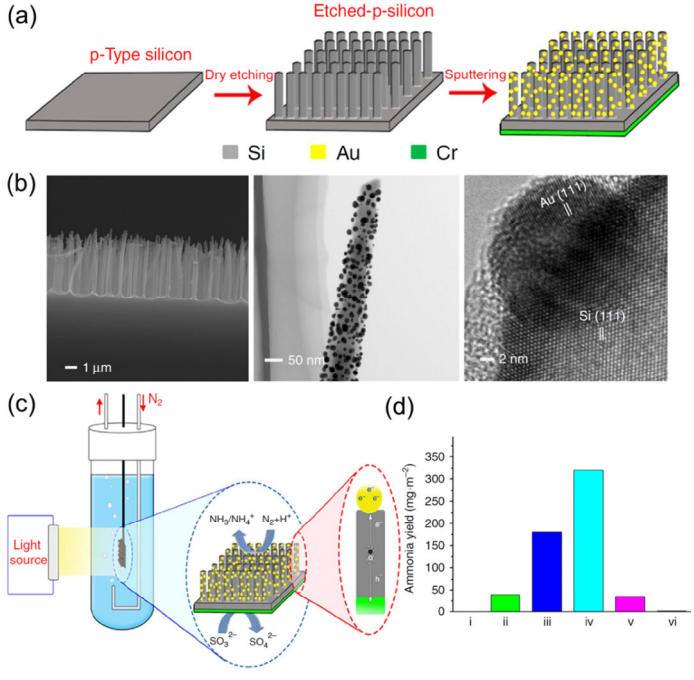

Figure 12 (a) Schematic preparation process of Au/black-Si/Cr photoelectrode. (b) (left) Cross-sectional view SEM, (middle) TEM and (right) HRTEM images of Au/black-Si/Cr photoelectrode. (c) Schematic illustration of the setup for photoelectrochemical NRR. (d) Photocatalytic NRR activity comparison over 24 h on (i) p-type silicon, (ii) black-Si, (iii) Au/black-Si, (iv) Au/black-Si/Cr and (v) Au/Si/Cr photoelectrodes after illumination with two suns and (vi) Au/black-Si/Cr photoelectrode in dark. Reproduced with permission from Ref. [109], © Nature Publishing Group 2016.

lamp irradiation and with continuously N_2 bubbling (Fig. 12(c)). The Au nanoparticles decorated black Si nanowire arrays with large surface area can effectively enhance the scattering and absorption of

light and facilitate the transfer of photo-generated electrons and holes. As presented in Fig. 12(d), the Au/black-Si/Cr photoelectrode exhibited the highest ammonia yield compared to other photoelectrodes. Although the efficiencies of state-of-the-art photoelectrochemical systems for artificial nitrogen fixation are still too low in practice, there is much scope to improve these systems for producing ammonia on a large scale.

4 Advances in electrocatalytic nitrogen fixation

Reducing nitrogen to ammonia with renewable electricity power is particular attractive due to its eco-friendliness, simple equipment, moderate efficiency as well as controllable selectivity by applying different potentials. Especially, the electrochemical process can proceed at room temperature and ambient pressure using the abundant N_2 and water on the Earth as source materials, leading to the low cost and zero carbon emission (Fig. 13). In 1985, Pickett and Talarmin reported the electrosynthesis of ammonia at ambient conditions through controlled-potential electrolysis of trans-$[W(N_2)_2(PMe_2Ph)_4]$ but with very low yield of ammonia [110]. Afterwards, Furuya et al. presented a series of inorganic electrocatalysts loaded on gas-diffusion electrodes to reduce N_2 to ammonia [111]. The best catalyst ZnSe exhibited a current efficiency of 2.24% for ammonia production at −0.5 V vs. RHE (reversible hydrogen electrode) in 1 M KOH solution. Since then, the development of electrocatalytic nitrogen fixation was almost stagnant until some relative studies emerged very recently. In this section, we focus on the recent achievements in electrochemical NRR in aqueous solution under ambient conditions. Table 2 provides the performance comparison of representative electrocatalysts for electrochemical N_2 conversion.

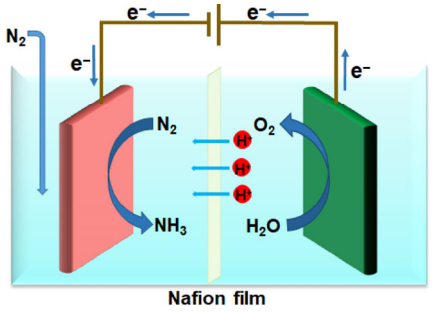

Figure 13 Illustration of electrocatalytic NRR process in aqueous solution at ambient conditions.

4.1 Metal electrocatalysts

4.1.1 *Noble metal electrocatalysts (Ru, Rh, Pt, Au, and Pd)*

In 2000, Kordali et al. reported that electrocatalytic NRR was able to take place on a Ru loaded carbon felt cathode in KOH aqueous solution with a Faradaic efficiency of 0.28% [112]. The NH_3 production began at a small overpotential of 0.08 V. The NH_3 generation rate reached the maximum value at −1.02 V vs. Ag/AgCl and afterwards it was decreased owing to the enhanced H_2 adsorption on electrode surface. The rate of NH_3 synthesis increased with the increase of temperature in accordance to the Arrhenius equation. The maximum reaction rate and current efficiency reached 1.3 $\mu g \cdot cm^{-2} \cdot h^{-1}$ at −1.02 V and 0.92% at −0.96 V, respectively. Wessling et al. prepared randomly-structured Ti felts covered by Ru and Rh by electroplating method. Both Ru and Rh coatings could boost electrochemical NH_3 synthesis, and Ru gave the higher activity [113].

Table 2 Summary of previously-reported catalysts for electrochemical NRR to NH_3 in aqueous solution under mild conditions

Catalyst	Electrolyte	Conditions	Ammonia yield (potential vs. RHE)	Faradaic efficiency (%) (potential vs. RHE)	Stability (retention of NH_3 yield)	Testing method	Reference
ZnSe	1 M KOH	25 °C AP[b]	417.60 $\mu g \cdot cm^{-2} \cdot h^{-1}$ (−1.0 V)	1.30 (−1.0 V)	—	Nessler's reagent	[111]
Ru/C	2 M KOH	20 °C AP[b]	0.21 $\mu g \cdot cm^{-2} \cdot h^{-1}$ (−1.1 V)	0.28 (−1.1 V)	—	Ion chromatography Phenate method	[112]
Ru/Ti	0.5 M H_2SO_4	30 °C	7.78 $\mu g \cdot cm^{-2} \cdot h^{-1}$ (−0.2 V)	—	—	Salicylic acid method	[113]
Ru SAs/N–C	0.05 M H_2SO_4	RT[a] AP[b]	120.9 $\mu g \cdot mg_{cat.}^{-1} \cdot h^{-1}$ (−0.2 V)	29.60 (−0.2 V)	12 h (> 93%)	Indophenol blue method	[128]
Rh ultrathin nanosheets	0.1 M KOH	RT[a] AP[b]	23.88 $\mu g \cdot mg_{cat.}^{-1} \cdot h^{-1}$ (−0.2 V)	0.217 (−0.2 V)	7,000 s	Phenolhypochlorite method	[114]
Pt/C	0.1 M Li_2SO_4	80 °C AP[b]	60.72 $\mu g \cdot cm^{-2} \cdot h^{-1}$ (voltage: 1.2 V)	0.83 (voltage: 1.2 V)	—	Nessler's reagent	[115]
Pt/C	NH_4^+/H^+ conducting Nafion-211 membrane	RT[a] 1 atm	7.39×10^{-3} $\mu g \cdot cm^{-2} \cdot h^{-1}$ (voltage: 1.6 V)	0.52 (voltage: 1.6 V)	—	Nessler's reagent	[116]
Au nanorods	0.1 M KOH	RT[a] AP[b]	1.648 $\mu g \cdot cm^{-2} \cdot h^{-1}$ (−0.2 V)	3.88 (−0.2 V)	18 h	Ammonia colorimetric assay kit Nessler's reagent	[117]
AuHNCs	0.5 M $LiClO_4$	RT[a] AP[b]	3.9 $\mu g \cdot cm^{-2} \cdot h^{-1}$ (−0.5 V)	30.20 (−0.4 V)	60 h	Ion chromatography Nessler's reagent	[118]
Au/TiO_2	0.1 M HCl	RT[a] AP[b]	21.4 $\mu g \cdot mg_{cat.}^{-1} \cdot h^{-1}$ (−0.2 V)	8.11 (−0.2 V)	2 h	Indophenol blue method	[119]
a-Au/CeO_x-RGO	0.1 M HCl	RT[a] AP[b]	8.3 $\mu g \cdot mg_{cat.}^{-1} \cdot h^{-1}$ (−0.2 V)	10.00 (−0.2 V)	2 h	Indophenol blue method	[120]
Pd/C	0.1 M Phosphate buffer solution	RT[a] AP[b]	4.5 $\mu g \cdot mg_{cat.}^{-1} \cdot h^{-1}$ (0.1 V)	8.20 (0.1 V)	3 h	Indophenol blue method	[121]
$Pd_{0.2}Cu_{0.8}$/rGO	0.1 M KOH	RT[a] AP[b]	2.8 $\mu g \cdot mg_{cat.}^{-1} \cdot h^{-1}$ (−0.2 V)	~ 4.10 (−0.2 V)	2 h	Indophenol blue method	[122]
(110)-oriented Mo nanofilm	0.01M H_2SO_4	RT[a] AP[b]	0.111 $\mu g \cdot cm^{-2} \cdot h^{-1}$ (−0.49 V)	0.72 (−0.29V)	—	Indophenol blue method	[123]
Porous Ni	0.01 M H_2SO_4 with 10% 2-propanol	RT[a] AP[b]	0.998 $\mu g \cdot cm^{-2} \cdot h^{-1}$ (−3.6 V)	0.089 (−3.6 V)	—	Indophenol method	[124]
PEBCD/C	0.5 M Li_2SO_4	25 °C AP[b]	1.58 $\mu g \cdot cm^{-2} \cdot h^{-1}$ (−0.5 V)	2.58 (−0.5 V)	36 h (82.2%)	Nessler's reagent	[129]

(Continued)

Catalyst	Electrolyte	Conditions	Ammonia yield (potential vs. RHE)	Faradaic efficiency (%) (potential vs. RHE)	Stability (retention of NH_3 yield)	Testing method	Reference
PCN-NVs	0.1 M HCl	20 °C AP[b]	8.09 $\mu g \cdot mg_{cat.}^{-1} \cdot h^{-1}$ (−0.2 V)	11.59 (−0.2 V)	8 h	Indophenol blue method	[130]
N–C derived from ZIF-8	0.1 M KOH	RT[a] AP[b]	3.4 $\mu mmol \cdot cm^{-2} \cdot h^{-1}$ (−0.3 V)	10.20 (−0.3V)	18 h	Indophenol blue method	[131]
Porous N–C	0.1 M KOH	RT[a] AP[b]	15.7 $\mu g \cdot mg_{cat.}^{-1} \cdot h^{-1}$ (−0.2 V)	1.45 (−0.2 V)	—	Indophenol blue method	[132]
B-graphene	0.05 M H_2SO_4	RT[a] AP[b]	9.8 $\mu g \cdot cm^{-2} \cdot h^{-1}$ (−0.5 V)	10.8 (−0.5 V)	10 h (96%)	Indophenol blue method	[133]
B_4C	0.5 M H_2SO_4	RT[a] AP[b]	26.57 $\mu g \cdot mg_{cat.}^{-1} \cdot h^{-1}$ (−0.75 V)	15.95 (−0.75 V)	14 h	Indophenol blue method	[134]
Fe_2O_3/CNTs	Diluted $KHCO_3$	20 °C AP[b]	0.22 $\mu g \cdot cm^{-2} \cdot h^{-1}$ (voltage: 2.0 V)	~ 0.15 (voltage: 2.0 V)	6 h	Ion selective electrode Salicylic acid method	[135]
Fe_2O_3 nanorods	0.1 M Na_2SO_4	RT[a] AP[b]	15.9 $\mu g \cdot mg_{cat.}^{-1} \cdot h^{-1}$ (−0.8 V)	0.94 (−0.8 V)	12 h	Indophenol blue method	[136]
Fe_3O_4/Ti	0.1 M Na_2SO_4	RT[a] AP[b]	0.2 $\mu mmol \cdot cm^{-2} \cdot h^{-1}$ (−0.4 V)	2.6 (−0.4 V)	18 h	Indophenol blue method	[137]
TiO_2/Ti	0.1 M Na_2SO_4	RT[a] AP[b]	0.33 $\mu mmol \cdot cm^{-2} \cdot h^{-1}$ (−0.7 V)	2.5 (−0.7 V)	30 h (90.2%)	Indophenol blue method	[138]
TiO_2/rGO	0.1 M Na_2SO_4	RT[a] AP[b]	15.13 $\mu g \cdot mg_{cat.}^{-1} \cdot h^{-1}$ (−0.9 V)	3.3 (−0.9 V)	12 h	Indophenol blue method	[139]
Cr_2O_3 microspheres	0.1 M Na_2SO_4	RT[a] AP[b]	25.3 $\mu g \cdot mg_{cat.}^{-1} \cdot h^{-1}$ (−0.9 V)	6.78 (−0.9 V)	10 h	Indophenol blue method	[140]
MoO_3 nanosheets	0.1 M HCl	RT[a] AP[b]	29.43 $\mu g \cdot mg_{cat.}^{-1} \cdot h^{-1}$ (−0.5 V)	1.9 (−0.3 V)	24 h	Indophenol blue method	[141]
Nb_2O_5 nanofibers	0.1 M HCl	RT[a] AP[b]	43.6 $\mu g \cdot mg_{cat.}^{-1} \cdot h^{-1}$ (−0.55 V)	9.26 (−0.55 V)	30 h	Indophenol blue method	[142]
SnO_2/CC	0.1 M Na_2SO_4	RT[a] AP[b]	0.53 $\mu mmol \cdot cm^{-2} \cdot h^{-1}$ (−0.7 V)	2.17 (−0.7 V)	20 h	Indophenol blue method	[143]
$Bi_4V_2O_{11}/CeO_2$	0.1 M HCl	RT[a] AP[b]	23.21 $\mu g \cdot mg_{cat.}^{-1} \cdot h^{-1}$ (−0.2 V)	10.16 (−0.2 V)	4 h	Indophenol blue method	[144]
MoS_2	0.1 M Na_2SO_4	RT[a] AP[b]	5.39 $\mu g \cdot cm^{-2} \cdot h^{-1}$ (−0.5 V)	1.17 (−0.5 V)	26 h	Salicylic acid method	[145]
VN nanowires	0.1 M HCl	RT[a] AP[b]	15.18 $\mu g \cdot cm^{-2} \cdot h^{-1}$ (−0.3 V)	3.58 (−0.3 V)	30 h	Indophenol blue method	[146]
VN nanoparticles	—	80 °C 1 atm	1.19 $\mu mmol \cdot cm^{-2} \cdot h^{-1}$ (−0.1 V)	6.0 (−0.1 V)	—	Nessler's reagent	[147]
Mo_2N nanorods	0.1 M HCl	RT[a] AP[b]	78.4 $\mu g \cdot mg_{cat.}^{-1} \cdot h^{-1}$ (−0.3 V)	4.50 (−0.3 V)	30 h	Indophenol blue method	[148]

[a]RT denotes room temperature, [b]AP denotes atmosphere pressure.

Ultrathin Rh nanosheets were used for electrocatalytic NRR, as shown in Figs. 14(a) and 14(b) [114]. A relatively high NH_3 production yield of 23.88 $\mu g \cdot mg_{cat.}^{-1} \cdot h^{-1}$ and favorable selectivity without N_2H_4 generation at low potential (−0.2 V vs. RHE) were achieved, superior to most of the reported NRR electrocatalysts. Lan et al. reported artificial ammonia synthesis on Pt electrode from air and H_2O with supplied electricity, showing an optimal ammonia production rate of 60.72 $\mu g \cdot cm^{-2} \cdot h^{-1}$ with a Faradaic efficiency of 0.83% at −1.2 V (80 °C) and 7.39×10^{-3} $\mu g \cdot cm^{-2} \cdot h^{-1}$ at −1.6 V with a Faradaic efficiency of 0.52% at room temperature [115, 116].

In 2016, Yan et al. reported a three-electrode catalytic system with tetrahexahedral Au nanorods loaded on carbon paper as cathode (Figs. 15(a) and 15(b)) [117]. The tetrahexahedral structure endowed Au a relatively good electrocatalytic NRR activity, owing to the exposed high-index (210) and (310) facets, which provided a large number of active sites to capture and activate N_2 molecules. The NRR began to occur at −0.05 V vs. RHE on the tetrahexahedral Au nanorods in 0.1 M KOH aqueous solution. As shown in Fig. 15(c), the maximum ammonia formation rate was 1.648 $\mu g \cdot cm^{-2} \cdot h^{-1}$ accompanied with a $N_2H_4 \cdot H_2O$ production rate of 0.102 $\mu g \cdot cm^{-2} \cdot h^{-1}$ at −0.2 V vs. RHE. According to DFT calculations, the NRR process preferably followed the alternating hydrogenation mechanism

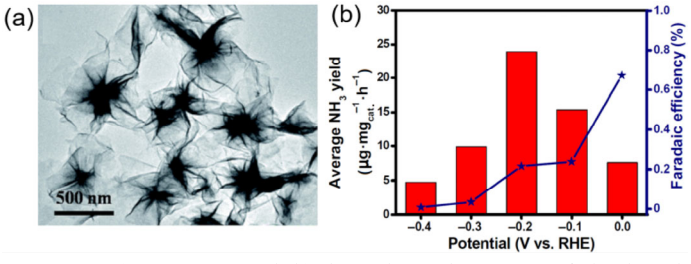

Figure 14 (a) TEM image and (b) electrochemical NRR tests of ultrathin Rh nanosheets. Reproduced with permission from Ref. [114], © Royal Society of Chemistry 2018.

(Fig. 15(d)). Hollow gold nanocages (AuHNCs) in Fig. 15(e) were also used for electrocatalytic NRR [118]. The highest Faradaic efficiency of AuHNCs for ammonia production was able to reach 30.2% at −0.4 V vs. RHE, much better than other Au nanostructures such as Au nanorods (AuNRs), Au nanospheres (AuNSs) and Au nanocubes (AuNCs), owing to the increased surface area and confinement effects (Fig. 15(f)).

Ultrafine metal nanoparticles were often supported on metal oxides to avoid the agglomeration. Yan et al. prepared Au sub-nanoclusters

(≈ 0.5 nm) embedded on TiO_2, which exhibited a high and stable ammonia production rate of 21.4 $\mu g \cdot mg_{cat.}^{-1} \cdot h^{-1}$ with a measured Faradaic efficiency of 8.11% at −0.2 V vs. RHE [119]. The electrocatalytic abilities of three Au nanostructures with different sizes embedded on TiO_2 were investigated and the smallest Au on TiO_2 exhibited the best performance. This was ascribed to the small-sized metal clusters with high surface energy boosted the formation of Au–O–Ti bonding on the TiO_2 support. The electroneutral N_2 was more easily to absorb on partially positive-charged Au active centers than the positively charged H^+, leading to the high efficiency of NRR but not the HER. A distal associate pathway was proposed for the electrocatalytic NRR process in this system. It is believed that the surface atoms of amorphous material in disorder and metastable state could lead to more dangling bonds and high unsaturated coordination sites, which is often the active sites of catalytic reaction. Recently, amorphous Au nanoparticles loaded on CeO_x/reduced graphite oxide (a-Au/CeO_x-RGO) was prepared and exhibited a high ammonia yield of 8.3 $\mu g \cdot mg_{cat.}^{-1} \cdot h^{-1}$ at −0.2 V vs. RHE with a high Faradaic efficiency of 10.10% [120]. The enhanced electrocatalytic activity was mainly attributed to the structural distortion and abundant active sites of the metastable amorphous Au.

Apart from Ru, Rh, Pt and Au, Pd is also a widely-studied noble metal electrocatalyst. A recent work reported the electrochemical NRR proceeded on Pd nanoparticles dispersed on carbon black (Pd/C) in phosphate buffer solution (Fig. 16(a)) [121]. The ammonia production rate and Faradaic efficiency of Pd/C were up to ~ 4.5 $\mu g \cdot mg_{cat.}^{-1} \cdot h^{-1}$ and 8.2% at −0.1 V vs. RHE, respectively. Compared with Au/C and Pt/C, Pd/C provided superior NRR performance at −0.05 V vs. RHE (Fig. 16(b)). DFT calculations indicated the N_2 hydrogenation on *in-situ* generated α-Pd hydride followed a Grotthuss-like hydride transfer mechanism, leading to the lower free energy barrier of rate-limiting step (from N_2 to $*N_2H$) (Fig. 16(c)). To decrease the cost and improve the catalytic activities, Yan et al. prepared amorphous PdCu alloy nanoclusters anchored on rGO for electrocatalytic NRR [122]. The optimal bimetallic $Pd_{0.2}Cu_{0.8}$/rGO showed a yield of 2.80 $\mu g \cdot mg_{cat.}^{-1} \cdot h^{-1}$ at −0.2 V vs. RHE, excelling those of monometallic counterparts (Pd/rGO and Cu/rGO).

4.1.2 *Non-noble metal electrocatalysts (Mo, Ni)*

The high cost and scarcity of noble metal electrocatalysts impede their large scale commercial applications. Hence, there is a growing desire to explore low-cost, and earth-abundant materials (such as non-precious metals) to replace noble metals. Previous theoretical calculations predicted that Mo could serve as a promising non-noble metal catalyst for electrochemical ammonia synthesis [34, 38]. Recently, Wang et al. [123] demonstrated the electrochemical NRR proceeded on (110)-oriented Mo nanofilm electrode in 0.01 M H_2SO_4 aqueous solution, exhibiting a Faradaic efficiency of 0.72% at an overpotential of 0.14 V. The Mo nanofilms with different main exposed facets showed different activities for electrocatalytic NRR, indicating that the morphology and the orientation of crystal phase played a key role in the NRR catalytic activity. Notably, appropriate electrolyte medium is also important for NH_3 electro-synthesis at mild conditions. In 2016, Kim and his coworkers reported that the use of porous Ni as electrode and 2-propanol as electrolyte medium was in favor of NH_3 electro-synthesis [124]. The porous Ni electrode gave the highest Faradaic efficiency of 0.89% in the optimal electrolyte of 2-propanol and water mixture (9:1, v/v).

4.1.3 *Single-atom electrocatalysts*

Single-atom catalysts have drawn extensive attention in heterogeneous catalysis owing to the maximum atomic utilization and enhanced catalytic activities [125, 126]. The single-atom catalysts consisting of isolated metal single atoms anchored on the support surfaces can exhibit unique chemical and physical properties. However, there are few reports on the use of single-atom catalysts for electrocatalytic NRR.

In 2017, Chen and coworkers investigated the potential of different single metal atoms anchored on defective boron nitride (BN) monolayer for electrocatalytic NRR by DFT calculations [127]. Single Mo atoms supported on defective BN monolayer was predicted to have the best electrocatalytic NRR activity, owing to the favorable

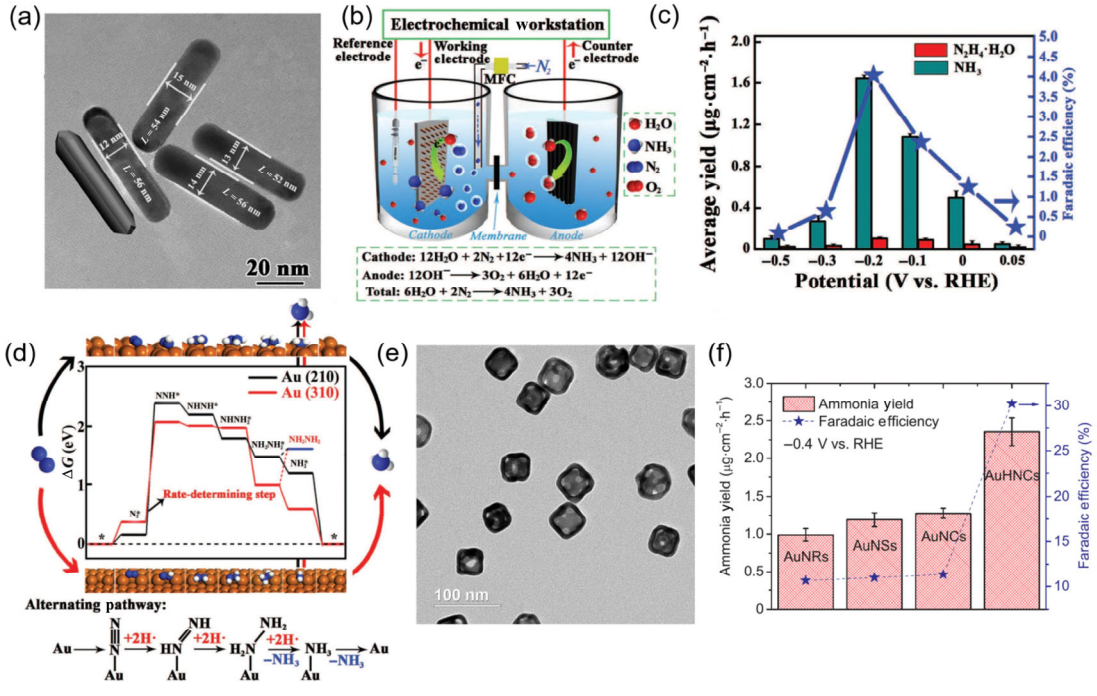

Figure 15 (a) TEM image of tetrahexahedral Au nanorods. (b) Schematic for electrocatalytic NRR (MFC is a mass flow controller, membrane is a Nafion-211 film). (c) Yield rates of ammonia (cyan), hydrazine hydrate (red), and Faradaic efficiencies (blue) at given potentials. (d) Free energy diagram and alternating hydriding pathways for NRR on Au (210) and Au (310) at equilibrium potential. Reproduced with permission from Ref. [117], © Wiley-VCH 2016. (e) TEM image of AuHNCs. (f) NH_3 production rates and Faradaic efficiencies of various Au nanostructures at −0.4 V vs. RHE in 0.5 M $LiClO_4$ aqueous solution. Reproduced with permission from Ref. [118], © Elsevier 2018.

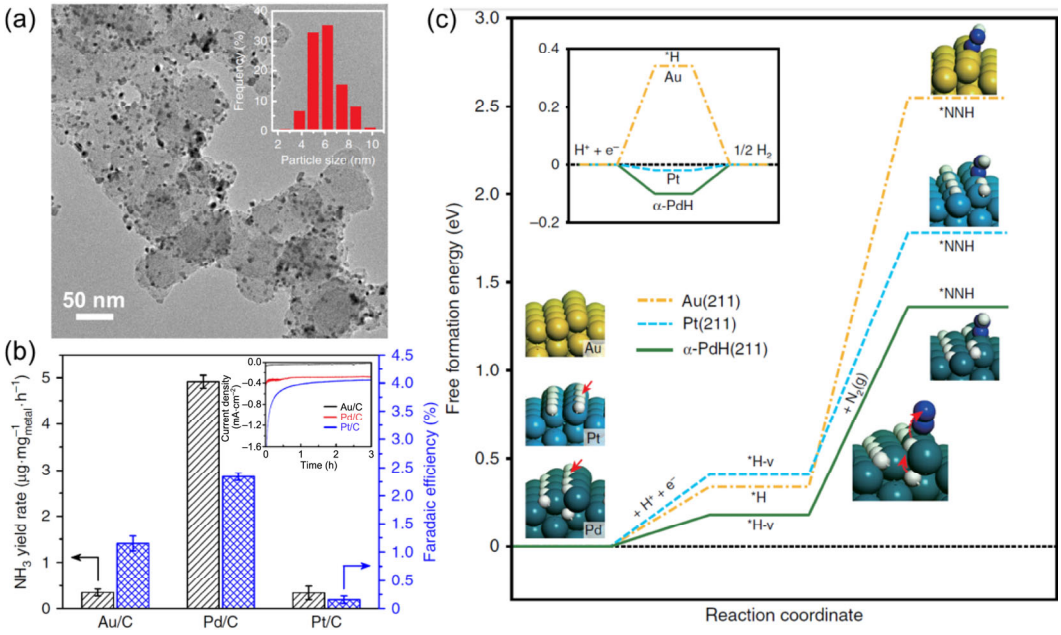

Figure 16 (a) TEM image of Pd/C catalyst. (b) Ammonia yield rates and Faradaic efficiencies of Au/C, Pt/C, and Pd/C catalysts. (c) Free energy diagrams of HER (inset) and the relevant steps of NRR on the (211) surfaces of Au, Pt, and α-PdH. Reproduced with permission from Ref. [121], © Nature Publishing Group 2018.

adsorption and activation of N_2, the selective stabilization of N_2H^* and the destabilization of NH_2^* on single Mo atom. Theoretical results showed that the NRR was proceeded by an enzymatic mechanism with a low overpotential of 0.19 V. Recently, Zeng et al. prepared Ru single atoms on N-doped carbon (Ru SAs/N–C) for electrochemical NRR [128], which exhibited a high Faradaic efficiency of 29.6% for NH_3 production and a yield rate of 120.9 $\mu g \cdot mg_{cat.}^{-1} \cdot h^{-1}$ at −0.2 V vs. RHE. Theoretical calculations indicated that this process followed the distal pathway.

4.2 Non-metal electrocatalysts

Intensive research efforts have been directed towards the cost reduction of electrocatalysis systems through the development of inexpensive electrocatalysts without the employment of precious metals. In recent years, metal-free catalysts and non-noble catalysts have drawn much attention among researchers as promising alternatives to the conventional metal based catalysts. It has been found that a combination of rich active sites, enhanced N_2 adsorption/activation, high conductivity and good stability is essential for durable and active NRR electrocatalysts. Examples include carbon-based materials and transition metal compounds, such as oxides, sulfides and nitrides, as summarized below.

4.2.1 Polymeric and carbonaceous electrocatalysts

Wang et al. reported that Li^+ incorporation into poly(N-ethyl-benzene-1, 2, 4, 5-tetracarboxylic diimide) electrocatalyst (PEBCD) dramatically enhanced the selectivity of N_2 electro-reduction [129]. Experimental results and DFT calculations demonstrated that NRR process could be effectively promoted and HER process could be decelerated by the association of Li^+ ions with the O atoms in the PEBCD matrix. The optimal NH_3 formation rate was 9.29 $\times 10^{-4}$ $mol \cdot m^{-2} \cdot h^{-1}$ with a Faradaic efficiency of 2.85% at 25 °C. Figure 17(b) provides the possible NRR mechanism with an alternative pathway: $[A] \cdot N \equiv N \rightarrow [A] \cdot NH=NH \rightarrow [A] \cdot NH_2=NH_2 \rightarrow [A] \cdot NH_3 \cdots NH_3 \rightarrow [A] \cdot NH_3 + NH_3 \rightarrow [A] + 2NH_3$. This result indicates a new way for NH_3 synthesis from N_2 and H_2O by the rational design of electro-active polymers.

The potential of nano-carbon materials as electrocatalyst materials have also been investigated. Nevertheless, the nature of carbon materials itself cannot meet the requirements, because the exposure of graphitic edge plane alone cannot lead to improved NRR activity, while structural defects or heteroatom doping are considered as a necessity. Many research works have demonstrated that vacancies (such as OVs and NVs) play an important role in the chemisorption and activation of inert N_2 molecules [81, 87, 102]. This is because the defective surface can provide coordinatively unsaturated sites for N_2 chemisorption and then the electrons trapped by vacancies could be injected into the antibonding orbital of adsorbed N_2, weakening the $N \equiv N$ bond for the activation of N_2 [55, 81, 102]. Recently, metal-free polymeric carbon nitride with rich NVs (PCN-NVs) was reported as an effective electrocatalyst for NRR [130]. Theoretical calculations suggested the introduction of nitrogen heteroatoms could create a net positive charge on the adjacent carbon atoms, resulting in the favorable adsorption and activation of N_2 on PCN-NVs (Fig. 17(c), top). As depicted in the free energy diagram (Fig. 17(c), bottom), the lowest energy pathways for NRR is the alternating hydrogenation mechanism. Consequently, the PCN-NVs achieved a NH_3 production rate of 8.09 $\mu g \cdot mg_{cat.}^{-1} \cdot h^{-1}$ with a Faradaic efficiency of 11.59%, which is ~ 10 times higher than that of PCN without nitrogen vacancies (Fig. 17(d)). Recently, N-doped highly disordered carbon derived from metal-organic framework (ZIF-8) was used as electrocatalyst for NRR in 0.1 M KOH solution and achieved a NH_3 yield of 3.4×10^{-6} $mol \cdot cm^{-2} \cdot h^{-1}$ with a Faradaic efficiency of 10.2% at −0.3 V vs. RHE [131]. Similarly, the electrocatalytic NRR performance of N-doped hierarchically porous carbon was investigated, showing a NH_3 yield of up to 15.7 $\mu g \cdot mg_{cat.}^{-1} \cdot h^{-1}$ and a NH_3 selectivity of 1.45% at −0.2 V vs. RHE [132].

Using boron-doped graphene (BG), Zheng et al. reported that N_2 could be reduced to NH_3 with a yield rate of 9.8 $\mu g \cdot m^{-2} \cdot h^{-1}$ and a Faradaic efficiency of 10.8% at −0.5 V vs. RHE [133]. This N_2 conversion activity was attributed to the favorable N_2 adsorption on positively charged boron atoms and the prohibition of H^+ binding on electron-deficient boron sites that retarded the HER process. Theoretical calculations suggest that the distal pathway is more feasible than other pathways and the BC_3-type bond in BG plays an important role in promoting NRR among several types of BG structures (BC_3, BC_2O, BCO_2) (Fig. 18(b)). Sun et al. showed the good electrocatalytic activity of boron carbide (B_4C) nanosheets for

NRR at ambient conditions (Fig. 18(c)) [134], achieving a NH_3 production rate of 26.57 $\mu g \cdot mg_{cat.}^{-1} \cdot h^{-1}$ with a Faradaic efficiency of 15.95% at −0.75 V vs. RHE. DFT calculations predict that the NRR process on B_4C prefers the alternating pathway in associative mechanism, with $*NH_2–*NH_2 \rightarrow *NH_2–*NH_3$ as the rate-limiting step (Fig. 18(d)).

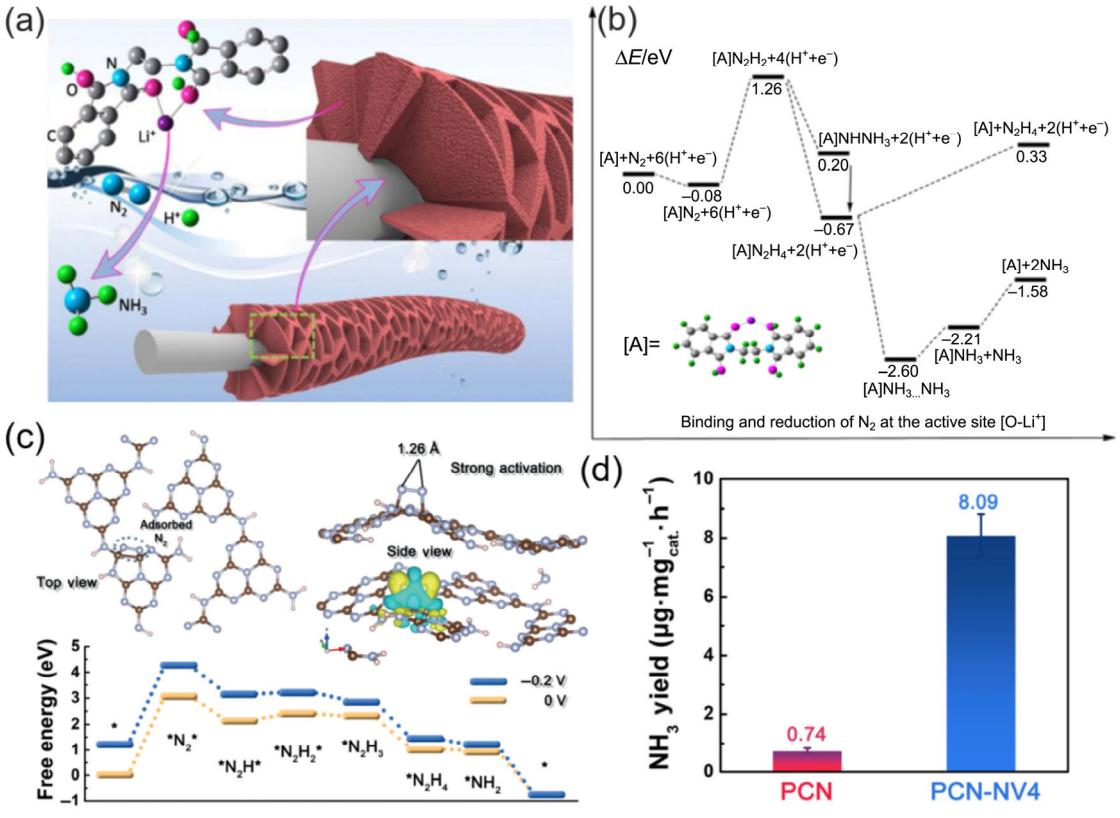

Figure 17 (a) Schematic electrochemical NRR process on PEBCD. (b) Predicted relative energies for NRR at the [O-Li$^+$] active site. The chemical potential of [H^+ + e^-] is defined by the binding energy of a single hydrogen atom in H_2. Reproduced with permission from Ref. [129], © American Chemical Society 2017. (c) The N_2 adsorption geometry on PCN-NVs, the charge density difference of N_2-adsorbed PCN-NVs, and the free energy diagram for NRR on PCN-NVs at equilibrium potential. (d) NH_3 yields on pristine PCN and PCN-NV4 at −0.2 V vs. RHE. Reproduced with permission from Ref. [130], © Wiley-VCH 2018.

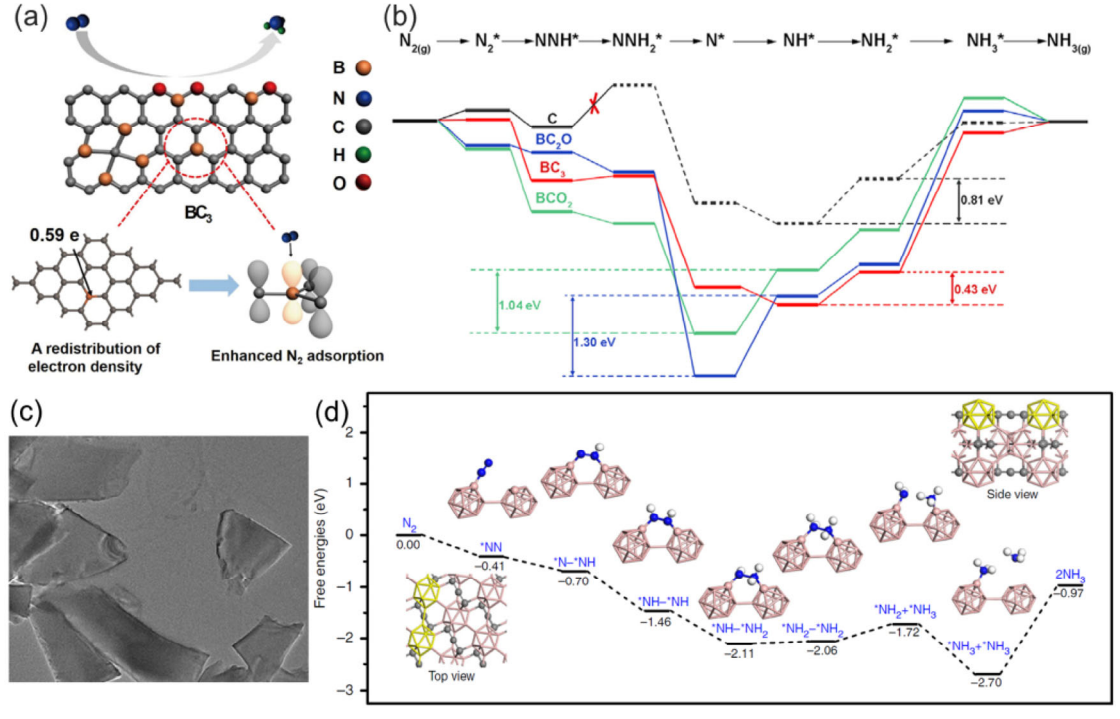

Figure 18 (a) Schematic of the atomic orbitals of BC_3 in BG for binding N_2. (b) Free energy diagrams of NRR on BC_3, BC_2O, BCO_2, and C, respectively. Reproduced with permission from Ref. [133], © Elsevier 2018. (c) TEM image of B_4C nanosheets. (d) DFT calculated energy profiles for the electrocatalytic NRR on B_4C (110) surface starting from the end-on adsorption structure. Color code: blue, N; rose, B; gray, C; white, H; the asterisk * denotes an adsorption site. Reproduced with permission from Ref. [134], © Nature Publishing Group 2018.

4.2.2 *Metal oxides based electrocatalysts*

Besides the metal-free carbonaceous electrocatalysts discussed above, metal oxides based composites also exhibited great potential in N_2 reduction. As depicted in Fig. 19(a), Centi et al. presented a non-conventional electrocatalytic cell using carbon paper loaded with iron oxide supported carbon nanotubes (Fe_2O_3-CNTs) as cathode [135]. It provides the possibility for electrochemical NH_3 synthesis under mild conditions with an ammonia generation rate of 2.2×10^{-3} g·m^{-2}·h^{-1} (Fig. 19(b)). Recently, Fe_2O_3 nanorods were used as electrocatalyst for NRR and exhibited an improved ammonia yield of 15.9 μg·mg$_{cat.}^{-1}$·h^{-1} at 0.8 V vs. RHE with a Faradaic efficiency of 0.94% in neutral electrolyte [136]. Compared to Fe_2O_3, spinel Fe_3O_4 nanorods delivered a better electrocatalytic NRR activity because of the higher electronic conductivity [137]. The electrochemical reduction of N_2 to NH_3 on TiO_2 nanosheets in neutral media was also demonstrated [138]. Sun et al. found that the TiO_2/rGO hybrids could act as an efficient electrocatalyst to convert N_2 into NH_3 [139], showing a NH_3 yield rate of 15.13 μg·mg$_{cat.}^{-1}$·h^{-1} at −0.90 V vs. RHE with a Faradaic efficiency of 3.3% in 0.1 M Na_2SO_4 aqueous solution. Lately, multishelled hollow Cr_2O_3 microspheres were also used for electrocatalytic NRR in neutral electrolytes [140], delivering a Faradaic efficiency of 6.78% and a NH_3 production rate of 25.3 μg·mg$_{cat.}^{-1}$·h^{-1} at −0.9 V vs. RHE. Sun et al. discovered that MoO_3 nanosheets could exhibit a NH_3 yield of 29.43 μg·mg$_{cat.}^{-1}$·h^{-1} with a Faradaic efficiency of 1.9%, which is attributed to the effective N_2 adsorption on the outermost Mo atoms [141]. Nb_2O_5 nanofibers as another noble-metal-free electrocatalyst exhibited remarkable NH_3 yield rate (43.6 μg·mg$_{cat.}^{-1}$·h^{-1}) and Faradaic efficiency (9.26%) at −0.55 V vs. RHE in 0.1 M HCl, outperforming the most reported NRR electrocatalysts [142]. A main-group metal oxide (SnO_2) was also utilized as electrocatalyst for NRR, achieving a NH_3 yield of 4.03 μg·mg$_{cat.}^{-1}$·h^{-1} with a Faradaic efficiency of 2.17% at −0.7 V vs. RHE in 0.1 M Na_2SO_4 [143]. Yu and coworkers synthesized a noble-metal-free $Bi_4V_2O_{11}$/CeO_2 hybrid with amorphous phase (BVC-A) by electrospinning and subsequent calcination for electrochemical NRR (Fig. 19(c)) [144]. CeO_2 could retard the heat transfer and contributed to the amorphization of $Bi_4V_2O_{11}$. $Bi_4V_2O_{11}$ with abundant defects trapped electrons and facilitated the adsorption/activation of inert N_2 molecules. Meanwhile, the band alignment between CeO_2 and $Bi_4V_2O_{11}$ was conducive to the rapid interfacial charge transfer. As displayed in Fig. 19(d), the $Bi_4V_2O_{11}$/CeO_2 hybrid presented a NH_3 yield of 23.21 μg·mg$_{cat.}^{-1}$·h^{-1} and a Faradaic efficiency of 10.16 %.

4.2.3 *Other metal compounds based electrocatalysts (sulfides, nitrides)*

Lately, Sun and co-workers reported the utilization of MoS_2 as electrocatalyst for NRR at ambient conditions [145]. DFT calculations predicted that the edge of MoS_2 could act as electrocatalytically active site. The energy barrier of potential-determining step (PDS) on MoS_2 edge site is 0.68 eV without external potential, much lower than that of flat surfaces of common metals (1–1.5 eV). The deformation charge density of *NNH indicates the charge transfer from N_2 to electropositive Mo-edge, which is conductive to the activation of the N≡N triple bond. The MoS_2 nanosheet array grown on carbon cloth (MoS_2/CC) exhibited a NH_3 production rate of 8.08×10^{-11} mol·cm^{-1}·s^{-1} with a Faradaic efficiency of 1.17% at −0.5 V vs. RHE in 0.1 M Na_2SO_4 solution.

Apart from metal sulphides, metal nitrides were also employed for NRR. VN nanowire array on carbon cloth showed a Faradaic efficiency of 3.58% for NRR at −0.5 V vs. RHE in 0.1 M HCl electrolyte [146]. Very recently, Xu et al. explored the electrocatalytic activity and the mechanism of NRR on VN nanoparticles [147]. The authors performed a series of *in-situ* and *ex-situ* characterizations, indicating that the active species were $VN_{0.7}O_{0.45}$ and the NRR mechanism was proposed to be a Mars–van Krevelen mechanism. The surface N close to the surface O was confirmed to be the active site. Mo_2N nanorods were also reported as an effective catalyst for selective NRR in 0.1 M HCl solution, achieving a Faradaic efficiency of 4.5% and a NH_3 yield of 78.4 μg·mg$_{cat.}^{-1}$·h^{-1} at −0.3 V vs. RHE [148].

5 Strategies for developing advanced N_2 fixation systems

5.1 Rational design of reaction cells

For photochemical N_2 fixation, the reaction system utilizing

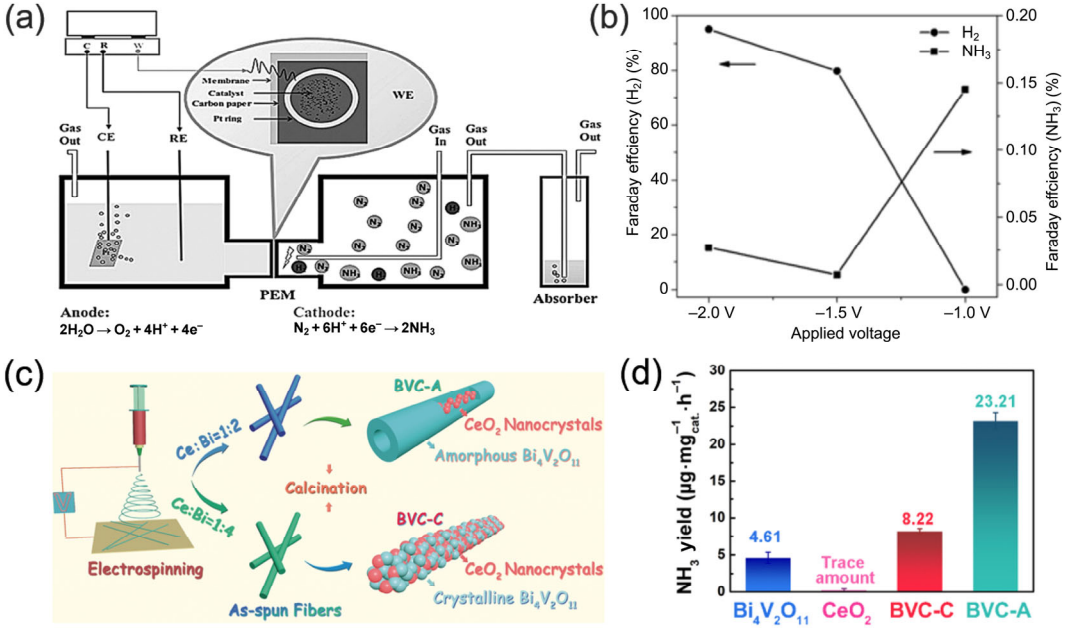

Figure 19 (a) Schematic view of the electrocatalytic flow reactor for NH_3 synthesis on Fe_2O_3-CNTs, with the cathode cell operating under electrolyte-less condition (gas phase). PEM denotes proton exchange membrane. (b) Faradaic efficiencies for NH_3 and H_2 generation at different applied potentials. Reproduced with permission from Ref. [135], © Wiley-VCH 2017. (c) Scheme of preparing BVC-A and $Bi_4V_2O_{11}$/CeO_2 hybrid with crystalline phase (BVC-C). (d) NH_3 yields of different catalysts at −0.2 V vs. RHE. Reproduced with permission from Ref. [144], ©Wiley-VCH 2018.

powdered semiconductor nanoparticles dispersed in N_2-saturated aqueous solutions can only use a single cell, which may suffer from the reverse reaction or re-oxidization of the product. An alternative solution is to fabricate a reaction system based on single cell or dual-compartment H-cell configurations containing photoanode, photocathode and electrolyte. As shown in Fig. 10, the ammonia yield of dual-compartment H-cell system is usually higher than that of single cell system, benefited from the effective inhibition of undesirable reactions.

In aqueous electrocatalytic N_2 fixation systems, generally there are three main cell configurations, namely, single chamber cell, dual-compartment H-cell and polymer electrolyte membrane (PEM)–type cell [17]. In 2006, a metal-free polyaniline catalyst was first used to synthesize ammonia in aqueous solution using single chamber cell at various conditions [149]. However, the ammonia production at atmospheric pressure is much lower than that at high pressure. Afterwards, Han et al. used porous Ni to catalyze N_2 reduction in a single chamber cell [124]. Notably, the author anticipated that the ammonia yield could be further improved by reasonably designing the cell configuration. Inside the single chamber cell, the produced ammonia will possibly be re-oxidized on the anode. In contrast, the dual-compartment H-cell can avoid this problem. Yan et al. reported the electrocatalytic NRR of Au nanorods in 0.1 M KOH solution based on a H-type cell, as shown in Fig. 15(b) [117]. Recently, there have been many electrocatalytic NRR research works based on dual-compartment H-cell systems [118–123, 128–134, 136–148]. The presence of working electrode and reference electrode in the cathodic chamber makes the applied voltage more precise. Moreover, the cathode and anode are separated by ion exchange membrane, which effectively inhibits the occurrence of side reactions. However, this system suffers from the ammonia/ammonium crossover effect [17]. Therefore, the ammonia concentration in both cathodic and anodic electrolytes should be measured. Another kind of reaction cell is PEM-type cell, which is seldom reported so far. As shown in Fig. 19(a), electrocatalytic NRR on Fe_2O_3/CNTs was achieved in a PEM-type cell, in which $KHCO_3$ solution was employed as anodic electrolyte to provide protons. This reaction system is favorable to the separation of ammonia, but exhibits a relatively low ammonia yield.

5.2 The effects of pH value in aqueous electrolytes

In photocatalytic N_2 fixation systems, some research works have investigated the effects of pH value on the performance of N_2 fixation. The results showed that the ammonia yields in acidic solutions were normally higher than those in neutral solutions. Wang et al. demonstrated that the photocatalytic ammonia production rate on ultrathin MoS_2 was up to 83 $\mu g \cdot h^{-1} \cdot L^{-1}$ in acidic solution (pH = 3.5), which is 6 times higher that in neutral solution [98]. It was also demonstrated that BiO quantum dots could produce more ammonia in acidic conditions than that in neutral solution [77]. This is possibly because the acidic solutions can provide more protons to reduce the kinetic barrier of nitrogen fixation. However, it is notable that many catalysts may be unstable and tend to decompose rapidly in acidic solutions.

The pH value of electrocatalytic NRR systems can also be adjusted by introducing acidic, neutral or alkaline electrolytes, such as dilute H_2SO_4, HCl, Na_2SO_4, $KHCO_3$, KOH aqueous solutions, etc. Chen and coworkers investigated the influences of different pH values on the electrocatalytic NRR performance of Fe_2O_3/CNTs catalysts [150]. The highest ammonia production rate and Faradaic efficiency were obtained in 0.5 M KOH solution, and the lowest ammonia yield rate and Faradaic efficiency were obtained in 0.25 M $KHSO_4$. These results indicate the pH value of electrolyte has a great impact on NH_3 generation. The low N_2 conversion rate in acidic solution was attributed to the HER process promoted by the high proton concentration. In alkaline electrolyte, water is the main proton source, thus the HER is significantly suppressed by the low proton concentration. Feng et al. reported the improvement of NRR selectivity on Pd/C catalyst by using phosphate buffer solution (pH = 7.2) to suppress the competing HER process [121], possibly because the high energy barriers for mass and charge transfer in phosphate buffer solution is not conducive to the kinetics of HER.

6 Challenges and perspectives

Photocatalytic and electrocatalytic artificial nitrogen fixation have drawn rising research interests owing to the following merits: (i) the NH_3 synthesis can be realized by using abundant N_2 and H_2O as raw materials under mild conditions, leading to the lower cost as well as the mitigation of energy crisis; (ii) the NRR process with zero-carbon emission can efficiently alleviate environmental issues such as global warming resulting from CO_2; (iii) it can provide a potential route to store clean and renewable solar energy and electricity in the form of a hydrogen carrier and carbon-free fuel (NH_3).

However, the progress of heterogeneous catalytic nitrogen fixation faces great obstacles, such as the intrinsic inertia of N_2 molecules, the weak binding strength of N_2 to the heterogeneous catalysts, the characteristics of multi-electron and multi-proton participated pathways. In addition, the ammonia production is normally accompanied by the simultaneous generation of hydrogen and hydrazine, resulting in a very low selectivity towards NH_3. More importantly, current understanding on the fundamental mechanisms of N_2 photo-reduction and electro-reduction is still very limited due to the considerably complicated reaction process.

To promote the development of heterogeneous nitrogen fixation under ambient conditions, here we put forward some perspectives on how to further improve the performance of photocatalytic and electrocatalytic NRR systems:

(1) The design of more efficient, cost-effective, environment-friendly and robust catalysts is very desirable. It is essential to develop novel technologies for nanomaterial synthesis, because the variant compositions and morphologies of nanostructured materials (such as quantum dots, nanowires, mesoporous films and so on) play an important role in enhancing the catalytic nitrogen fixation performance. The interface control, surface engineering, chemical modification and so on are promising methods for the optimization of catalyst performance. Especially, defective catalyst surface has an enormous impact on the catalytic performance. Compared to the flat bulk surfaces, the roughened surfaces with rich defects and doped heteroatoms possess larger catalytic active surface area and considerably more low-coordination sites (such as vacancies, corners, edges and steps), which have greatly enhanced intrinsic catalytic activity. Dong et al. demonstrated that the introduction of NVs could endow g-C_3N_4 with excellent photocatalytic NRR activity. In contrast, the photocatalytic activity was greatly inhibited when the NVs were occupied by Pd nanoparticles [87]. In addition, the electronic and geometric effects induced by chemical modification can give rise to the appropriate variation and adjustment of binding strengths of reaction intermediates on catalyst surface, giving better catalytic properties. The construction of heterogeneous single-atom catalysts is another inviting approach for promoting the NRR performance due to the high activities of single metal atoms. For example, Ru-single atoms were used for NRR and exhibited improved ammonia yield and selectivity [128]. The good news is single-atom catalysts could be conveniently synthesized from metal-organic frameworks or metal-organic complexes [151–153].

(2) To uncover the obscure fundamental mechanisms of heterogeneous NRR processes is important. N_2 reduction is regarded as a considerably complicated multi-step reaction, and many details still

remain unclear. The DFT method has been utilized as a powerful tool to predict the possible active sites, the rate-determining step and the intermediates of the reaction. The effective combination of theoretical analysis and experimental results is advantageous to reveal the reaction mechanisms of NRR at molecular scale. Especially, more attention should be paid to building reasonable models closer to the actual reaction systems. Meanwhile the theoretical computation based on materials genome method and "big data" approaches could provide a feasible way to design novel catalysts.

(3) Advanced characterization techniques, such as spherical aberration corrected transmission electron microscopy (ACTEM), *in-situ* synchrotron radiation (SR) techniques, *in-situ* X-ray photoelectron spectroscopy (XPS), *in-situ* diffuse reflectance Fourier transform infrared spectroscopy (DRFTIRS), and *in-situ* electron paramagnetic resonance spectroscopy (EPR) are suggested to be used for the precise investigation of the active sites as well as the intermediates structure during the reaction processes. Moreover, isotope labelling is an effective and direct method for detecting the source and pathway of reaction products. *In-situ* FTIR has also be utilized to monitor the time-dependent change of the functional groups on catalyst surfaces (such as BiOBr, Bi_5O_7Br nanotubes and CuCr LDH nanosheets), which is helpful to confirm the ammonia formation process [81, 83, 102]. Shao and coworkers employed surface-enhanced infrared absorption spectroscopy (SEIRAS) to detect the reactive species of electrochemical NRR on Au thin film for investigating the detailed reaction mechanism [154]. *Ex-situ* XPS, *operando* X-ray absorption spectroscopy and ^{15}N isotope labelling were used to explore the mechanism of nitrogen fixation reaction in detail [147]. Recently, as a promising method, single entity electrochemistry has been pioneered for identifying the intrinsic catalytic performances of an individual catalyst particle [155–158]. For example, Long et al. detected the collision events and quantified the electron transfer of a single N719@TiO_2 nanoparticle by a novel ultrasensitive photoelectrochemical system [159].

In summary, this tutorial review presented the developing course of photocatalytic and electrocatalytic N_2 conversion for ammonia synthesis in aqueous solution, indicating the possibility of producing NH_3 from abundant N_2, H_2O, solar energy as well as renewable electricity. Despite facing great challenges, the heterogeneous catalytic synthesis of ammonia under mild conditions holds a great promise to reduce our reliance on fossil fuels and mitigate the impact of climate change.

Acknowledgements

This work was supported by the National Key R&D Program of China (Nos. 2017YFA0208200, 2016YFB0700600, and 2015CB659300), the National Natural Science Foundation of China (NSFC) (Nos. 21872069, 51761135104, and 21573108), the Natural Science Foundation of Jiangsu Province (Nos. BK20180008 and BK20150571), High-Level Entrepreneurial and Innovative Talents Program of Jiangsu Province, and the Fundamental Research Funds for the Central Universities of China (No. 020514380146).

References

[1] Canfield, D. E.; Glazer, A. N.; Falkowski, P. G. The evolution and future of Earth's nitrogen cycle. *Science* **2010**, *330*, 192–196.
[2] Hoffman, B. M.; Lukoyanov, D.; Yang, Z. Y.; Dean, D. R.; Seefeldt, L. C. Mechanism of nitrogen fixation by nitrogenase: The next stage. *Chem. Rev.* **2014**, *114*, 4041–4062.
[3] Thamdrup, B. New pathways and processes in the global nitrogen cycle. *Annu. Rev. Ecol. Evol. Syst.* **2012**, *43*, 407–428.
[4] Jia, H. P.; Quadrelli, E. A. Mechanistic aspects of dinitrogen cleavage and hydrogenation to produce ammonia in catalysis and organometallic chemistry: Relevance of metal hydride bonds and dihydrogen. *Chem. Soc. Rev.* **2014**, *43*, 547–564.
[5] Bazhenova, T. A.; Shilov, A. E. Nitrogen fixation in solution. *Coord. Chem. Rev.* **1995**, *144*, 69–145.
[6] Tanaka, H.; Mori, H.; Seino, H.; Hidai, M.; Mizobe, Y.; Yoshizawa, K. DFT study on chemical N_2 fixation by using a Cubane-type $RuIr_3S_4$ cluster: Energy profile for binding and reduction of N_2 to ammonia via Ru−N−NH_x (x = 1−3) intermediates with unique structures. *J. Am. Chem. Soc.* **2008**, *130*, 9037–9047.
[7] MacKay, B. A.; Fryzuk, M. D. Dinitrogen coordination chemistry: On the biomimetic borderlands. *Chem. Rev.* **2004**, *104*, 385–402.
[8] Gruber, N.; Galloway, J. N. An Earth-system perspective of the global nitrogen cycle. *Nature* **2008**, *451*, 293–296.
[9] Connor, G. P.; Holland, P. L. Coordination chemistry insights into the role of alkali metal promoters in dinitrogen reduction. *Catal. Today* **2017**, *286*, 21–40.
[10] Erisman, J. W.; Sutton, M. A.; Galloway, J.; Klimont, Z.; Winiwarter, W. How a century of ammonia synthesis changed the world. *Nat. Geosci.* **2008**, *1*, 636–639.
[11] Kandemir, T.; Schuster, M. E.; Senyshyn, A.; Behrens, M.; Schlögl, R. The Haber–Bosch process revisited: On the real structure and stability of "ammonia iron" under working conditions. *Angew. Chem., Int. Ed.* **2013**, *52*, 12723–12726.
[12] Tanaka, H.; Nishibayashi, Y.; Yoshizawa, K. Interplay between theory and experiment for ammonia synthesis catalyzed by transition metal complexes. *Acc. Chem. Res.* **2016**, *49*, 987–995.
[13] Tanabe, Y.; Nishibayashi, Y. Developing more sustainable processes for ammonia synthesis. *Coord. Chem. Rev.* **2013**, *257*, 2551–2564.
[14] Howard, J. B.; Rees, D. C. Structural basis of biological nitrogen fixation. *Chem. Rev.* **1996**, *96*, 2965–2982.
[15] Rees, D. C.; Tezcan, F. A.; Haynes, C. A.; Walton, M. Y.; Andrade, S.; Einsle, O.; Howard, J. B. Structural basis of biological nitrogen fixation. *Philos. Trans. Roy. Soc. A* **2005**, *363*, 971–984.
[16] Chen, X. Z.; Li, N.; Kong, Z. Z.; Ong, W. J.; Zhao, X. J. Photocatalytic fixation of nitrogen to ammonia: State-of-the-art advancements and future prospects. *Mater. Horiz.* **2018**, *5*, 9–27.
[17] Cui, X. Y.; Tang, C.; Zhang, Q. A review of electrocatalytic reduction of dinitrogen to ammonia under ambient conditions. *Adv. Energy Mater.* **2018**, *8*, 1800369.
[18] Shipman, M. A.; Symes, M. D. Recent progress towards the electrosynthesis of ammonia from sustainable resources. *Catal. Today* **2017**, *286*, 57–68.
[19] Soria, J.; Conesa, J. C.; Augugliaro, V.; Palmisano, L.; Schiavello, M.; Sclafani, A. Dinitrogen photoreduction to ammonia over titanium dioxide powders doped with ferric ions. *J. Phys. Chem.* **1991**, *95*, 274–282.
[20] Zhu, D.; Zhang, L. H.; Ruther, R. E.; Hamers, R. J. Photo-illuminated diamond as a solid-state source of solvated electrons in water for nitrogen reduction. *Nat. Mater.* **2013**, *12*, 836–841.
[21] Christianson, J. R.; Zhu, D.; Hamers, R. J.; Schmidt, J. R. Mechanism of N_2 reduction to NH_3 by aqueous solvated electrons. *J. Phys. Chem. B* **2013**, *118*, 195–203.
[22] Bauer, N. Theoretical pathways for the reduction of N_2 molecules in aqueous media: Thermodynamics of $N_2H_n^1$. *J. Phys. Chem.* **1960**, *64*, 833–837.
[23] Shilov, A. E. Catalytic reduction of molecular nitrogen in solutions. *Russ. Chem. Bull.* **2003**, *52*, 2555–2562.
[24] Li, J.; Li, H.; Zhan, G. M.; Zhang, L. Z. Solar water splitting and nitrogen fixation with layered bismuth oxyhalides. *Acc. Chem. Res.* **2017**, *50*, 112–121.
[25] Li, L.; Wang, Y. C.; Vanka, S.; Mu, X. Y.; Mi, Z. T.; Li, C. J. Nitrogen photofixation over III-nitride nanowires assisted by ruthenium clusters of low atomicity. *Angew. Chem.* **2017**, *129*, 8827–8831.
[26] Li, H.; Li, J.; Ai, Z. H.; Jia, F. L.; Zhang, L. Z. Oxygen vacancy-mediated photocatalysis of BiOCl: Reactivity, selectivity, and perspectives. *Angew. Chem., Int. Ed.* **2018**, *57*, 122–138.
[27] Giddey, S.; Badwal, S. P. S.; Kulkarni, A. Review of electrochemical ammonia production technologies and materials. *Int. J. Hydrogen Energy* **2013**, *38*, 14576–14594.
[28] Jewess, M.; Crabtree, R. H. Electrocatalytic nitrogen fixation for distributed fertilizer production. *ACS Sustainable Chem. Eng.* **2016**, *4*, 5855–5858.
[29] Singh, A. R.; Rohr, B. A.; Schwalbe, J. A.; Cargnello, M.; Chan, K.; Jaramillo, T. F.; Chorkendorff, I.; Nørskov, J. K. Electrochemical ammonia synthesis–the selectivity challenge. *ACS Catal.* **2017**, *7*, 706–709.
[30] van der Ham, C. J. M.; Koper, M. T. M.; Hetterscheid, D. G. H. Challenges in reduction of dinitrogen by proton and electron transfer. *Chem. Soc. Rev.* **2014**, *43*, 5183–5191.

[31] Guo, C. X.; Ran, J. R.; Vasileff, A.; Qiao, S. Z. Rational design of electrocatalysts and photo(electro)catalysts for nitrogen reduction to ammonia (NH_3) under ambient conditions. *Energy Environ. Sci.* **2018**, *11*, 45–56.

[32] Hoffman, B. M.; Dean, D. R.; Seefeldt, L. C. Climbing nitrogenase: Toward a mechanism of enzymatic nitrogen fixation. *Acc. Chem. Res.* **2009**, *42*, 609–619.

[33] Rod, T. H.; Logadottir, A.; Nørskov, J. K. Ammonia synthesis at low temperatures. *J. Chem. Phys.* **2000**, *112*, 5343–5347.

[34] Skúlason, E.; Bligaard, T.; Gudmundsdóttir, S.; Studt, F.; Rossmeisl, J.; Abild-Pedersen, F.; Vegge, T.; Jónsson, H.; Nørskov, J. K. A theoretical evaluation of possible transition metal electro-catalysts for N_2 reduction. *Phys. Chem. Chem. Phys.* **2012**, *14*, 1235–1245.

[35] Abghoui, Y.; Garden, A. L.; Howalt, J. G.; Vegge, T.; kúlason, E. Electroreduction of N_2 to ammonia at ambient conditions on mononitrides of Zr, Nb, Cr, and V: A DFT guide for experiments. *ACS Catal.* **2016**, *6*, 635–646.

[36] Abghoui, Y.; Garden, A. L.; Hlynsson, V. F.; Björgvinsdóttir, S.; Ólafsdóttir, H.; Skúlason, E. Enabling electrochemical reduction of nitrogen to ammonia at ambient conditions through rational catalyst design. *Phys. Chem. Chem. Phys.* **2015**, *17*, 4909–4918.

[37] Seh, Z. W.; Kibsgaard, J.; Dickens, C. F.; Chorkendorff, I.; Nørskov, J. K.; Jaramillo, T. F. Combining theory and experiment in electrocatalysis: Insights into materials design. *Science* **2017**, *355*, eaad4998.

[38] Montoya, J. H.; Tsai, C.; Vojvodic, A.; Nørskov, J. K. The challenge of electrochemical ammonia synthesis: A new perspective on the role of nitrogen scaling relations. *ChemSusChem* **2015**, *8*, 2180–2186.

[39] Back, S.; Jung, Y. On the mechanism of electrochemical ammonia synthesis on the Ru catalyst. *Phys. Chem. Chem. Phys.* **2016**, *18*, 9161–9166.

[40] Matanović, I.; Garzon, F. H.; Henson, N. J. Electro-reduction of nitrogen on molybdenum nitride: Structure, energetics, and vibrational spectra from DFT. *Phys. Chem. Chem. Phys.* **2014**, *16*, 3014–3026.

[41] Azofra, L. M.; Li, N.; MacFarlane, D. R.; Sun, C. H. Promising prospects for 2D d^2–d^4 M_3C_2 transition metal carbides (MXenes) in N_2 capture and conversion into ammonia. *Energy Environ. Sci.* **2016**, *9*, 2545–2549.

[42] Hisatomi, T.; Kubota, J.; Domen, K. Recent advances in semiconductors for photocatalytic and photoelectrochemical water splitting. *Chem. Soc. Rev.* **2014**, *43*, 7520–7535.

[43] Chang, X. X.; Wang, T.; Gong, J. L. CO_2 photo-reduction: Insights into CO_2 activation and reaction on surfaces of photocatalysts. *Energy Environ. Sci.* **2016**, *9*, 2177–2196.

[44] Chu, S.; Li, W.; Yan, Y. F.; Hamann, T.; Shih, I.; Wang, D. W.; Mi, Z. T. Roadmap on solar water splitting: Current status and future prospects. *Nano Futures* **2017**, *1*, 022001.

[45] Chen, X. B.; Mao, S. S. Titanium dioxide nanomaterials: Synthesis, properties, modifications, and applications. *Chem. Rev.* **2007**, *107*, 2891–2959.

[46] Yang, W. L.; Zhang, X. D.; Xie, Y. Advances and challenges in chemistry of two-dimensional nanosheets. *Nano Today* **2016**, *11*, 793–816.

[47] Guan, M. L.; Xiao, C.; Zhang, J.; Fan, S. J.; An, R.; Cheng, Q. M.; Xie, J. F.; Zhou, M.; Ye, B. J.; Xie, Y. Vacancy associates promoting solar-driven photocatalytic activity of ultrathin bismuth oxychloride nanosheets. *J. Am. Chem. Soc.* **2013**, *135*, 10411–10417.

[48] Kubacka, A.; Fernández-García, M.; Colón, G. Advanced nanoarchitectures for solar photocatalytic applications. *Chem. Rev.* **2012**, *112*, 1555–1614.

[49] Hou, W. B.; Cronin, S. B. A review of surface plasmon resonance-enhanced photocatalysis. *Adv. Funct. Mater.* **2013**, *23*, 1612–1619.

[50] Schrauzer, G. N.; Guth, T. D. Photolysis of water and photoreduction of nitrogen on titanium dioxide. *J. Am. Chem. Soc.* **1977**, *99*, 7189–7193.

[51] Bourgeois, S.; Diakite, D.; Perdereau, M. A study of TiO_2 powders as a support for the photochemical synthesis of ammonia. *React. Solids* **1988**, *6*, 95–104.

[52] Radford, P. P.; Francis, C. G. Photoreduction of nitrogen by metal doped titanium dioxide powders: A novel use for metal vapour techniques. *J. Chem. Soc. Chem. Commun.* **1983**, *24*, 1520–1521.

[53] Zhao, W. R.; Zhang, J.; Zhu, X.; Zhang, M.; Tang, J.; Tan, M.; Wang, Y. Enhanced nitrogen photofixation on Fe-doped TiO_2 with highly exposed (101) facets in the presence of ethanol as scavenger. *Appl. Catal., B Environ.* **2014**, *144*, 468–477.

[54] Vettraino, M.; Trudeau, M.; Lo, A. Y. H.; Schurko, R. W.; Antonelli, D. Room-temperature ammonia formation from dinitrogen on a reduced mesoporous titanium oxide surface with metallic properties. *J. Am. Chem. Soc.* **2002**, *124*, 9567–9573.

[55] Hirakawa, H.; Hashimoto, M.; Shiraishi, Y.; Hirai, T. Photocatalytic conversion of nitrogen to ammonia with water on surface oxygen vacancies of titanium dioxide. *J. Am. Chem. Soc.* **2017**, *139*, 10929–10936.

[56] Yang, J. H.; Guo, Y. Z.; Jiang, R. B.; Qin, F.; Zhang, H.; Lu, W. Z.; Wang, J. F.; Yu, J. C. High-efficiency "working-in-tandem" nitrogen photofixation achieved by assembling plasmonic gold nanocrystals on ultrathin titania nanosheets. *J. Am. Chem. Soc.* **2018**, *140*, 8497–8508.

[57] Ileperuma, O. A.; Tennakone, K.; Dissanayake, W. D. D. P. Photocatalytic behaviour of metal doped titanium dioxide: Studies on the photochemical synthesis of ammonia on Mg/TiO_2 catalyst systems. *Appl. Catal.* **1990**, *62*, L1–L5.

[58] Palmisano, L.; Augugliaro, V.; Sclafani, A.; Schiavello, M. Activity of chromium-ion-doped titania for the dinitrogen photoreduction to ammonia and for the phenol photodegradation. *J. Phys. Chem.* **1988**, *92*, 6710–6713.

[59] Ileperuma, O. A.; Thaminimulla, C. T. K.; Kiridena, W. C. B. Photoreduction of N_2 to NH_3 and H_2O to H_2 on metal doped TiO_2 catalysts (M = Ce, V). *Sol. Energy Mater. Sol. Cells* **1993**, *28*, 335–343.

[60] Linnik, O. P.; Kisch, H. Dinitrogen photofixation at ruthenium-modified titania films. *Mendeleev Commun.* **2008**, *18*, 10–11.

[61] Rusina, O.; Eremenko, A.; Frank, G.; Strunk, H. P.; Kisch, H. Nitrogen photofixation at nanostructured iron titanate films. *Angew. Chem., Int. Ed.* **2001**, *40*, 3993–3995.

[62] Chen, X. B.; Shen, S. H.; Guo, L. J.; Mao, S. S. Semiconductor-based photocatalytic hydrogen generation. *Chem. Rev.* **2010**, *110*, 6503–6570.

[63] Qu, Y. Q.; Duan, X. F. Progress, challenge and perspective of heterogeneous photocatalysts. *Chem. Soc. Rev.* **2013**, *42*, 2568–2580.

[64] Rao, N. N.; Dube, S.; Manjubala, Natarajan, P. Photocatalytic reduction of nitrogen over (Fe, Ru or Os)/TiO_2 catalysts. *Appl. Catal. B Environ.* **1994**, *5*, 33–42.

[65] Ranjit, K. T.; Varadarajan, T. K.; Viswanathan, B. Photocatalytic reduction of dinitrogen to ammonia over noble-metal-loaded TiO_2. *J. Photochem. Photobiol. A Chem.* **1996**, *96*, 181–185.

[66] Tennakone, K.; Wickramanayake, S.; Fernando, C. A. N.; Ileperuma, O. A.; Punchihewa, S. Photocatalytic nitrogen reduction using visible light. *J. Chem. Soc. Chem. Commun.* **1987**, *14*, 1078–1080.

[67] Lashgari, M.; Zeinalkhani, P. Photocatalytic N_2 conversion to ammonia using efficient nanostructured solar-energy-materials in aqueous media: A novel hydrogenation strategy and basic understanding of the phenomenon. *Appl. Catal. A Gen.* **2017**, *529*, 91–97.

[68] Khader, M. M.; Lichtin, N. N.; Vurens, G. H.; Salmeron, M.; Somorjai, G. A. Photoassisted catalytic dissociation of water and reduction of nitrogen to ammonia on partially reduced ferric oxide. *Langmuir* **1987**, *3*, 303–304.

[69] Ileperuma, O. A.; Kiridena, W. C. B.; Dissanayake, W. D. D. Photoreduction of nitrogen and water on montmorillonite clays loaded with hydrous ferric oxide. *J. Photochem. Photobiol. A Chem.* **1991**, *59*, 191–197.

[70] Hoshino, K.; Kuchii, R.; Ogawa, T. Dinitrogen photofixation properties of different titanium oxides in conducting polymer/titanium oxide hybrid systems. *Appl. Catal. B Environ.* **2008**, *79*, 81–88.

[71] Tennakone, K.; Fernando, C. A. N.; Wickramanayake, S.; Damayanthi, M. W. P.; Silva, L. H. K.; Wijeratne, W.; Illeperuma, O. A.; Punchihewa, S. Photocatalytic reduction of nitrogen to ammonia with coprecipitated Fe(III) and Ti(IV) hydrous oxides. *Sol. Energy Mater.* **1988**, *17*, 47–53.

[72] Tennakone, K.; Thaminimulla, C. T. K.; Bandara, J. M. S. Nitrogen photoreduction by vanadium(III)-substituted hydrous ferric oxide. *J. Photochem. Photobiol. A Chem.* **1992**, *68*, 131–135.

[73] Tennakone, K.; Thaminimulla, C. T. K.; Kiridena, W. C. B. Nitrogen photoreduction by coprecipitated hydrous oxides of samarium(III) and vanadium(III). *Langmuir* **1993**, *9*, 723–726.

[74] Tennakone, K.; Punchihewa, S.; Tantrigoda, R. Nitrogen photoreduction with cuprous chloride coated hydrous cuprous oxide. *Sol. Energy Mater.* **1989**, *18*, 217–221.

[75] Li, X. M.; Wang, W. Z.; Jiang, D.; Sun, S. M.; Zhang, L.; Sun, X. Efficient solar-driven nitrogen fixation over carbon–tungstic-acid hybrids. *Chem. -Eur. J.* **2016**, *22*, 13819–13822.

[76] Zhang, N.; Jalil, A.; Wu, D. X.; Chen, S. M.; Liu, Y. F.; Gao, C.; Ye, W.; Qi, Z. M.; Ju, H. X.; Wang, C. M. et al. Refining defect states in $W_{18}O_{49}$ by Mo doping: A strategy for tuning N_2 activation towards solar-driven nitrogen fixation. *J. Am. Chem. Soc.* **2018**, *140*, 9434–9443.

[77] Sun, S. M.; An, Q.; Wang, W. Z.; Zhang, L.; Liu, J. J.; Goddard III, W. A. Efficient photocatalytic reduction of dinitrogen to ammonia on bismuth monoxide quantum dots. *J. Mater. Chem. A* **2017**, *5*, 201–209.

[78] Hao, Y. C.; Dong, X. L.; Zhai, S. R.; Ma, H. C.; Wang, X. Y.; Zhang, X. F. Hydrogenated bismuth molybdate nanoframe for efficient sunlight-driven nitrogen fixation from air. *Chem. -Eur. J.* **2016**, *22*, 18722–18728.

[79] Mi, Y.; Zhou, M.; Wen, L. Y.; Zhao, H. P.; Lei, Y. A highly efficient visible-light driven photocatalyst: Two dimensional square-like bismuth oxyiodine nanosheets. *Dalton Trans.* **2014**, *43*, 9549–9556.

[80] Bhachu, D. S.; Moniz, S. J. A.; Sathasivam, S.; Scanlon, D. O.; Walsh, A.; Bawaked, S. M.; Mokhtar, M.; Obaid, A. Y.; Parkin, I. P.; Tang, J. W. et al. Bismuth oxyhalides: Synthesis, structure and photoelectrochemical activity. *Chem. Sci.* **2016**, *7*, 4832–4841.

[81] Li, H.; Shang, J.; Ai, Z. H.; Zhang, L. Z. Efficient visible light nitrogen fixation with BiOBr nanosheets of oxygen vacancies on the exposed {001} facets. *J. Am. Chem. Soc.* **2015**, *137*, 6393–6399.

[82] Li, H.; Shang, J.; Shi, J. G.; Zhao, K.; Zhang, L. Z. Facet-dependent solar ammonia synthesis of BiOCl nanosheets via a proton-assisted electron transfer pathway. *Nanoscale* **2016**, *8*, 1986–1993.

[83] Wang, S. Y.; Hai, X.; Ding, X.; Chang, K.; Xiang, Y. G.; Meng, X. G.; Yang, Z. X.; Chen, H.; Ye, J. H. Light-switchable oxygen vacancies in ultrafine Bi_5O_7Br nanotubes for boosting solar-driven nitrogen fixation in pure water. *Adv. Mater.* **2017**, *29*, 1701774.

[84] Bai, Y.; Ye, L. Q.; Chen, T.; Wang, L.; Shi, X.; Zhang, X.; Chen, D. Facet-dependent photocatalytic N_2 fixation of bismuth-rich Bi_5O_7I nanosheets. *ACS Appl. Mater. Interfaces* **2016**, *8*, 27661–27668.

[85] Ong, W. J.; Tan, L. L.; Ng, Y. H.; Yong, S. T.; Chai, S. P. Graphitic carbon nitride ($g\text{-}C_3N_4$)-based photocatalysts for artificial photosynthesis and environmental remediation: Are we a step closer to achieving sustainability? *Chem. Rev.* **2016**, *116*, 7159–7329.

[86] Naseri, A.; Samadi, M.; Pourjavadi, A.; Moshfegh, A. Z.; Ramakrishna, S. Graphitic carbon nitride ($g\text{-}C_3N_4$)-based photocatalysts for solar hydrogen generation: Recent advances and future development directions. *J. Mater. Chem. A* **2017**, *5*, 23406–23433.

[87] Dong, G. H.; Ho, W.; Wang, C. Y. Selective photocatalytic N_2 fixation dependent on $g\text{-}C_3N_4$ induced by nitrogen vacancies. *J. Mater. Chem. A* **2015**, *3*, 23435–23441.

[88] Wu, G.; Gao, Y.; Zheng, B. H. Template-free method for synthesizing sponge-like graphitic carbon nitride with a large surface area and outstanding nitrogen photofixation ability induced by nitrogen vacancies. *Ceram. Int.* **2016**, *42*, 6985–6992.

[89] Ma, H. Q.; Shi, Z. Y.; Li, S.; Liu, N. Large-scale production of graphitic carbon nitride with outstanding nitrogen photofixation ability via a convenient microwave treatment. *Appl. Surf. Sci.* **2016**, *379*, 309–315.

[90] Ma, H. Q.; Shi, Z. Y.; Li, Q.; Li, S. Preparation of graphitic carbon nitride with large specific surface area and outstanding N_2 photofixation ability via a dissolve-regrowth process. *J. Phys. Chem. Solids* **2016**, *99*, 51–58.

[91] Li, S. J.; Chen, X.; Hu, S. Z.; Li, Q.; Bai, J.; Wang, F. Infrared ray assisted microwave synthesis: A convenient method for large-scale production of graphitic carbon nitride with outstanding nitrogen photofixation ability. *RSC Adv.* **2016**, *6*, 45931–45937.

[92] Hu, S. Z.; Chen, X.; Li, Q.; Li, F. Y.; Fan, Z. P.; Wang, H.; Wang, Y. J.; Zheng, B. H.; Wu, G. Fe^{3+} doping promoted N_2 photofixation ability of honeycombed graphitic carbon nitride: The experimental and density functional theory simulation analysis. *Appl. Catal. B Environ.* **2017**, *201*, 58–69.

[93] Li, X. M.; Sun, X.; Zhang, L.; Sun, S. M.; Wang, W. Z. Efficient photocatalytic fixation of N_2 by KOH-treated $g\text{-}C_3N_4$. *J. Mater. Chem. A* **2018**, *6*, 3005–3011.

[94] Shiraishi, Y.; Shiota, S.; Kofuji, Y.; Hashimoto, M.; Chishiro, K.; Hirakawa, H.; Tanaka, S.; Ichikawa, S.; Hirai, T. Nitrogen fixation with water on carbon-nitride-based metal-free photocatalysts with 0.1% solar-to-ammonia energy conversion efficiency. *ACS Appl. Energy Mater.* **2018**, *1*, 4169–4177.

[95] Liu, Q. X.; Ai, L. H.; Jiang, J. MXene-derived TiO_2@C/$g\text{-}C_3N_4$ heterojunctions for highly efficient nitrogen photofixation. *J. Mater. Chem. A* **2018**, *6*, 4102–4110.

[96] Miyama, H.; Fujii, N.; Nagae, Y. Heterogeneous photocatalytic synthesis of ammonia from water and nitrogen. *Chem. Phys. Lett.* **1980**, *74*, 523–524.

[97] Ye, L. Q.; Han, C. Q.; Ma, Z. Y.; Leng, Y. M.; Li, J.; Ji, X. X.; Bi, D. Q.; Xie, H. Q.; Huang, Z. X. Ni_2P loading on $Cd_{0.5}Zn_{0.5}S$ solid solution for exceptional photocatalytic nitrogen fixation under visible light. *Chem. Eng. J.* **2017**, *307*, 311–318.

[98] Sun, S. M.; Li, X. M.; Wang, W. Z.; Zhang, L.; Sun, X. Photocatalytic robust solar energy reduction of dinitrogen to ammonia on ultrathin MoS_2. *Appl. Catal. B Environ.* **2017**, *200*, 323–329.

[99] Hu, S. Z.; Chen, X.; Li, Q.; Zhao, Y. F.; Mao, W. Effect of sulfur vacancies on the nitrogen photofixation performance of ternary metal sulfide photocatalysts. *Catal. Sci. Technol.* **2016**, *6*, 5884–5890.

[100] Cao, Y. H.; Hu, S. Z.; Li, F. Y.; Fan, Z. P.; Bai, J.; Lu, G.; Wang, Q. Photofixation of atmospheric nitrogen to ammonia with a novel ternary metal sulfide catalyst under visible light. *RSC Adv.* **2016**, *6*, 49862–49867.

[101] Tennakone, K.; Bandara, J. M. S.; Thaminimulla, C. T. K.; Jayatilake, W. D. W.; Ketipearachchi, U. S.; Ileperuma, O. A.; Priyadarshana, M. K. A. Photoreduction of dinitrogen to ammonia by ultrafine particles of iron hydroxide oxide (Fe(O)OH) formed by photohydrolysis of iron(II) bicarbonate. *Langmuir* **1991**, *7*, 2166–2168.

[102] Zhao, Y. F.; Zhao, Y. X.; Waterhouse, G. I. N.; Zheng, L. R.; Cao, X. Z.; Teng, F.; Wu, L. Z.; Tung, C. H.; O'Hare, D.; Zhang, T. R. Layered-double-hydroxide nanosheets as efficient visible-light-driven photocatalysts for dinitrogen fixation. *Adv. Mater.* **2017**, *29*, 1703828.

[103] Xu, C. M.; Qiu, P. X.; Li, L. Y.; Chen, H.; Jiang, F.; Wang, X. Bismuth subcarbonate with designer defects for broad-spectrum photocatalytic nitrogen fixation. *ACS Appl. Mater. Interfaces* **2018**, *10*, 25321–25328.

[104] Chen, H. M.; Chen, C. K.; Liu, R. S.; Zhang, L.; Zhang, J. J.; Wilkinson, D. P. Nano-architecture and material designs for water splitting photoelectrodes. *Chem. Soc. Rev.* **2012**, *41*, 5654–5671.

[105] Li, Z. S.; Luo, W. J.; Zhang, M. L.; Feng, J. Y.; Zou, Z. G. Photoelectrochemical cells for solar hydrogen production: Current state of promising photoelectrodes, methods to improve their properties, and outlook. *Energy Environ. Sci.* **2013**, *6*, 347–370.

[106] Oshikiri, T.; Ueno, K.; Misawa, H. Plasmon-induced ammonia synthesis through nitrogen photofixation with visible light irradiation. *Angew. Chem., Int. Ed.* **2014**, *53*, 9802–9805.

[107] Oshikiri, T.; Ueno, K.; Misawa, H. Selective dinitrogen conversion to ammonia using water and visible light through plasmon-induced charge separation. *Angew. Chem.* **2016**, *128*, 4010–4014.

[108] Li, C. C.; Wang, T.; Zhao, Z. J.; Yang, W. M.; Li, J. F.; Li, A.; Yang, Z. L.; Ozin, G. A.; Gong, J. L. Promoted fixation of molecular nitrogen with surface oxygen vacancies on plasmon–enhanced TiO_2 photoelectrodes. *Angew. Chem., Int. Ed.* **2018**, *57*, 5278–5282.

[109] Ali, M.; Zhou, F. L.; Chen, K.; Kotzur, C.; Xiao, C. L.; Bourgeois, L.; Zhang, X. Y.; MacFarlane, D. R. Nanostructured photoelectrochemical solar cell for nitrogen reduction using plasmon-enhanced black silicon. *Nat. Commun.* **2016**, *7*, 11335.

[110] Pickett, C. J.; Talarmin, J. Electrosynthesis of ammonia. *Nature* **1985**, *317*, 652–653.

[111] Furuya, N.; Yoshiba, H. Electroreduction of nitrogen to ammonia on gas-diffusion electrodes loaded with inorganic catalyst. *J. Electroanal. Chem. Int. Electrochem.* **1990**, *291*, 269–272.

[112] Kordali, V.; Kyriacou, G.; Lambrou, C. Electrochemical synthesis of ammonia at atmospheric pressure and low temperature in a solid polymer electrolyte cell. *Chem. Commun.* **2000**, *17*, 1673–1674.

[113] Kugler, K.; Luhn, M.; Schramm, J. A.; Rahimi, K.; Wessling, M. Galvanic deposition of Rh and Ru on randomly structured Ti felts for the electrochemical NH_3 synthesis. *Phys. Chem. Chem. Phys.* **2015**, *17*, 3768–3782.

[114] Liu, H. M.; Han, S. H.; Zhao, Y.; Zhu, Y. Y.; Tian, X. L.; Zeng, J. H.; Jiang, J. X.; Xia, B. Y.; Chen, Y. Surfactant-free atomically ultrathin rhodium nanosheet nanoassemblies for efficient nitrogen electroreduction. *J. Mater. Chem. A* **2018**, *6*, 3211–3217.

[115] Lan, R.; Tao, S. W. Electrochemical synthesis of ammonia directly from air and water using a $Li^+/H^+/NH_4^+$ mixed conducting electrolyte. *RSC Adv.* **2013**, *3*, 18016–18021.

[116] Lan, R.; Irvine, J. T. S.; Tao, S. W. Synthesis of ammonia directly from air and water at ambient temperature and pressure. *Sci. Rep.* **2013**, *3*, 1145.

[117] Bao, D.; Zhang, Q.; Meng, F. L.; Zhong, H. X.; Shi, M. M.; Zhang, Y.; Yan, J. M.; Jiang, Q.; Zhang, X. B. Electrochemical reduction of N_2 under ambient conditions for artificial N_2 fixation and renewable energy storage using N_2/NH_3 cycle. *Adv. Mater.* **2017**, *29*, 1604799.

[118] Nazemi, M.; Panikkanvalappil, S. R.; El-Sayed, M. A. Enhancing the rate of electrochemical nitrogen reduction reaction for ammonia synthesis under ambient conditions using hollow gold nanocages. *Nano Energy* **2018**, *49*, 316–323.

[119] Shi, M. M.; Bao, D.; Wulan, B. R.; Li, Y. H.; Zhang, Y. F.; Yan, J. M.; Jiang, Q. Au sub-nanoclusters on TiO_2 toward highly efficient and selective electrocatalyst for N_2 conversion to NH_3 at ambient conditions. *Adv. Mater.* **2017**, *29*, 1606550.

[120] Li, S. J.; Bao, D.; Shi, M. M.; Wulan, B. R.; Yan J. M.; Jiang, Q. Amorphizing of Au nanoparticles by CeO_x–RGO hybrid support towards highly efficient electrocatalyst for N_2 reduction under ambient conditions. *Adv. Mater.* **2017**, *29*, 1700001.

[121] Wang, J.; Yu, L.; Hu, L.; Chen, G.; Xin, H. L.; Feng, X. F. Ambient ammonia synthesis via palladium-catalyzed electrohydrogenation of dinitrogen at low overpotential. *Nat. Commun.* **2018**, *9*, 1795.

[122] Shi, M. M.; Bao, D.; Li, S. J.; Wulan, B. R.; Yan, J. M.; Jiang, Q. Anchoring PdCu amorphous nanocluster on graphene for electrochemical reduction of N_2 to NH_3 under ambient conditions in aqueous solution. *Adv. Energy Mater.* **2018**, *8*, 1800124.

[123] Yang, D. S.; Chen, T.; Wang, Z. J. Electrochemical reduction of aqueous nitrogen (N_2) at a low overpotential on (110)-oriented Mo nanofilm. *J. Mater. Chem. A* **2017**, *5*, 18967–18971.

[124] Kim, K.; Lee, N.; Yoo, C. Y.; Kim, J. N.; Yoon, H. C.; Han, J. I. Communication-electrochemical reduction of nitrogen to ammonia in 2-propanol under ambient temperature and pressure. *J. Electrochem. Soc.* **2016**, *163*, F610–F612.

[125] Ding, K. L.; Gulec, A.; Johnson, A. M.; Schweitzer, N. M.; Stucky, G. D.; Marks, L. D.; Stair, P. C. Identification of active sites in CO oxidation and water–gas shift over supported Pt catalysts. *Science* **2015**, *350*, 189–192.

[126] Jones, J.; Xiong, H. F.; DeLaRiva, A. T.; Peterson, E. J.; Pham, H.; Challa, S. R.; Qi, G.; Oh, S.; Wiebenga, M. H.; Hernández, X. I. P. et al. Thermally stable single-atom platinum-on-ceria catalysts via atom trapping. *Science* **2016**, *353*, 150–154.

[127] Zhao, J. X.; Chen, Z. F. Single Mo atom supported on defective boron nitride monolayer as an efficient electrocatalyst for nitrogen fixation: A computational study. *J. Am. Chem. Soc.* **2017**, *139*, 12480–12487.

[128] Geng, Z. G.; Liu, Y.; Kong, X. D.; Li, P.; Li, K.; Liu, Z. Y.; Du, J. J.; Shu, M.; Si, R.; Zeng, J. Achieving a record–high yield rate of 120.9 $\mu g_{NH_3} \cdot mg_{cat.}^{-1} \cdot h^{-1}$ for N_2 electrochemical reduction over Ru single–atom catalysts. *Adv. Mater.* **2018**, *30*, 1803498.

[129] Chen, G. F.; Cao, X. R.; Wu, S. Q.; Zeng, X. Y.; Ding, L. X.; Zhu, M.; Wang, H. H. Ammonia electrosynthesis with high selectivity under ambient conditions via a Li^+ incorporation strategy. *J. Am. Chem. Soc.* **2017**, *139*, 9771–9774.

[130] Lv, C. D.; Qian, Y. M.; Yan, C. S.; Ding, Y.; Liu, Y. Y.; Chen, G.; Yu, G. H. Defect engineering metal-free polymeric carbon nitride electrocatalyst for effective nitrogen fixation under ambient conditions. *Angew. Chem., Int. Ed.* **2018**, *57*, 10246–10250.

[131] Mukherjee, S.; Cullen, D. A.; Karakalos, S.; Liu, K. X.; Zhang, H.; Zhao, S.; Xu, H.; More, K. L.; Wang, G. F.; Wu, G. Metal-organic framework-derived nitrogen-doped highly disordered carbon for electrochemical ammonia synthesis using N_2 and H_2O in alkaline electrolytes. *Nano Energy* **2018**, *48*, 217–226.

[132] Yang, X. X.; Li, K.; Cheng, D. M.; Pang, W. L.; Lv, J. Q.; Chen, X. Y.; Zhang, H. Y.; Wu, X. L.; Tan, H. Q.; Wang, Y. H. et al. Nitrogen-doped porous carbon: Highly efficient trifunctional electrocatalyst for oxygen reversible catalysis and nitrogen reduction reaction. *J. Mater. Chem. A* **2018**, *6*, 7762–7769.

[133] Yu, X. M.; Han, P.; Wei, Z. X.; Huang, L. S.; Gu, Z. X.; Peng, S. J.; Ma, J. M.; Zheng, G. F. Boron-doped graphene for electrocatalytic N_2 reduction. *Joule* **2018**, *2*, 1610–1622.

[134] Qiu, W. B.; Xie, X. Y.; Qiu, J. D.; Fang, W. H.; Liang, R. P.; Ren, X.; Ji, X. Q.; Cui, G. W.; Asiri, A. M.; Cui, G. L. et al. High-performance artificial nitrogen fixation at ambient conditions using a metal-free electrocatalyst. *Nat. Commun.* **2018**, *9*, 3485.

[135] Chen, S. M.; Perathoner, S.; Ampelli, C.; Mebrahtu, C.; Su, D. S.; Centi, G. Electrocatalytic synthesis of ammonia at room temperature and atmospheric pressure from water and nitrogen on a carbon-nanotube-based electrocatalyst. *Angew. Chem.* **2017**, *129*, 2743–2747.

[136] Xiang, X. J.; Wang, Z.; Shi, X. F.; Fan, M. K.; Sun, X. P. Ammonia synthesis from electrocatalytic N_2 reduction under ambient conditions by Fe_2O_3 Nanorods. *ChemCatChem.* **2018**, *10*, 4530–4535.

[137] Liu, Q.; Zhang, X. X.; Zhang, B.; Luo, Y. L.; Cui, G. W.; Xie, F. Y.; Sun, X. P. Ambient N_2 fixation to NH_3 electrocatalyzed by a spinel Fe_3O_4 nanorod. *Nanoscale* **2018**, *10*, 14386–14389.

[138] Zhang, R.; Ren, X.; Shi, X. F.; Xie, F. Y.; Zheng, B. Z.; Guo, X. D.; Sun, X. P. Enabling effective electrocatalytic N_2 conversion to NH_3 by the TiO_2 nanosheets array under ambient conditions. *ACS Appl. Mater. Interfaces* **2018**, *10*, 28251–28255.

[139] Zhang, X. X.; Liu, Q.; Shi, X. F.; Asiri, A. M.; Luo, Y. L.; Sun, X. P.; Li, T. S. TiO_2 nanoparticles–reduced graphene oxide hybrid: An efficient and durable electrocatalyst toward artificial N_2 fixation to NH_3 under ambient conditions. *J. Mater. Chem. A* **2018**, *6*, 17303–17306.

[140] Zhang, Y.; Qiu, W. B.; Ma, Y. J.; Luo, Y. L.; Tian, Z. Q.; Cui, G. W.; Xie, F. Y.; Chen, L.; Li, T. S.; Sun, X. P. High-performance electrohydrogenation of N_2 to NH_3 catalyzed by multishelled hollow Cr_2O_3 microspheres under ambient conditions. *ACS Catal.* **2018**, *8*, 8540–8544.

[141] Han, J. R.; Ji, X. Q.; Ren, X.; Cui, G. W.; Li, L.; Xie, F. Y.; Wang, H.; Li, B. H.; Sun, X. P. MoO_3 nanosheets for efficient electrocatalytic N_2 fixation to NH_3. *J. Mater. Chem. A* **2018**, *6*, 12974–12977.

[142] Han, J. R.; Liu, Z. C.; Ma, Y. J.; Cui, G. W.; Xie, F. Y.; Wang, F. X.; Wu, Y. P.; Gao, S. Y.; Xu, Y. H.; Sun, X. P. Ambient N_2 fixation to NH_3 at ambient conditions: Using Nb_2O_5 nanofiber as a high-performance electrocatalyst. *Nano Energy* **2018**, *52*, 264–270.

[143] Zhang, L.; Ren, X.; Luo, Y. L.; Shi, X. F.; Asiri, A. M.; Li, T. S.; Sun, X. P. Ambient NH_3 synthesis via electrochemical reduction of N_2 over cubic sub-micron SnO_2 particles. *Chem. Commun.* **2018**, *54*, 12966–12969.

[144] Lv, C. D.; Yan, C. S.; Chen, G.; Ding, Y.; Sun, J. X.; Zhou, Y. S.; Yu, G. H. An amorphous noble–metal–free electrocatalyst that enables nitrogen fixation under ambient conditions. *Angew. Chem.* **2018**, *130*, 6181–6184.

[145] Zhang, L.; Ji, X. Q.; Ren, X.; Ma, Y. J.; Shi, X. F.; Tian, Z. Q.; Asiri, A. M.; Chen, L.; Tang, B.; Sun, X. P. Electrochemical ammonia synthesis via nitrogen reduction reaction on a MoS_2 catalyst: Theoretical and experimental studies. *Adv. Mater.* **2018**, *30*, 1800191.

[146] Zhang, X. P.; Kong, R. M.; Du, H. T.; Xia, L.; Qu, F. L. Highly efficient electrochemical ammonia synthesis via nitrogen reduction reactions on a VN nanowire array under ambient conditions. *Chem. Commun.* **2018**, *54*, 5323–5325.

[147] Yang, X.; Nash, J.; Anibal, J.; Dunwell, M.; Kattel, S.; Stavitski, E.; Attenkofer, K.; Chen, J. G.; Yan, Y. S.; Xu, B. J. Mechanistic insights into electrochemical nitrogen reduction reaction on vanadium nitride nanoparticles. *J. Am. Chem. Soc.* **2018**, *140*, 13387–13391.

[148] Ren, X.; Cui, G. W.; Chen, L.; Xie, F. Y.; Wei, Q.; Tian, Z. Q.; Sun, X. P. Electrochemical N_2 fixation to NH_3 under ambient conditions: Mo_2N nanorod as a highly efficient and selective catalyst. *Chem. Commun.* **2018**, *54*, 8474–8477.

[149] Köleli, F.; Röpke, T. Electrochemical hydrogenation of dinitrogen to ammonia on a polyaniline electrode. *Appl. Catal. B Environ.* **2006**, *62*, 306–310.

[150] Chen, S. M.; Perathoner, S.; Ampelli, C.; Mebrahtu, C.; Su, D. S.; Centi, G. Room-temperature electrocatalytic synthesis of NH_3 from H_2O and N_2 in a gas-liquid-solid three-phase reactor. *ACS Sustainable Chem. Eng.* **2017**, *5*, 7393–7400.

[151] Zhang, H. B.; Liu, G. G.; Shi, L.; Ye, J. H. Single-atom catalysts: Emerging multifunctional materials in heterogeneous catalysis. *Adv. Energy Mater.* **2018**, *8*, 1701343.

[152] Zhao, C. M.; Dai, X. Y.; Yao, T.; Chen, W. X.; Wang, X. Q.; Wang, J.; Yang, J.; Wei, S. Q.; Wu, Y.; Li, Y. D. Ionic exchange of metal-organic frameworks to access single nickel sites for efficient electroreduction of CO_2. *J. Am. Chem. Soc.* **2017**, *139*, 8078–8081.

[153] Yin, P. Q.; Yao, T.; Wu, Y.; Zheng, L. R.; Lin, Y.; Liu, W.; Ju, H. X.; Zhu, J. F.; Hong, X.; Deng, Z. X. et al. Single cobalt atoms with precise N-coordination as superior oxygen reduction reaction catalysts. *Angew. Chem., Int. Ed.* **2016**, *55*, 10800–10805.

[154] Yao, Y.; Zhu, S. Q.; Wang, H. J.; Li, H.; Shao, M. H. A spectroscopic study on the nitrogen electrochemical reduction reaction on gold and platinum surfaces. *J. Am. Chem. Soc.* **2018**, *140*, 1496–1501.

[155] Zhao, L. J.; Qian, R. C.; Ma, W.; Tian, H.; Long, Y. T. Electrocatalytic efficiency analysis of catechol molecules for NADH oxidation during nanoparticle collision. *Anal. Chem.* **2016**, *88*, 8375–8379.

[156] Xiao, X. Y.; Bard, A. J. Observing single nanoparticle collisions at an ultramicroelectrode by electrocatalytic amplification. *J. Am. Chem. Soc.* **2007**, *129*, 9610–9612.

[157] Peng, Y. Y.; Guo, D.; Ma, W.; Long, Y. T. Intrinsic Electrocatalytic activity of gold nanoparticles measured by single entity electrochemistry. *ChemElectroChem* **2018**, *5*, 2982–2985.

[158] Ma, H.; Ma, W.; Chen, J. F.; Liu, X. Y.; Peng, Y. Y.; Yang, Z. Y.; Tian, H.; Long, Y. T. Quantifying visible-light-induced electron transfer properties of single dye-sensitized ZnO entity for water splitting. *J. Am. Chem. Soc.* **2018**, *140*, 5272–5279.

[159] Peng, Y. Y.; Ma, H.; Ma, W.; Long, Y. T.; Tian, H. Single-nanoparticle photoelectrochemistry at a nanoparticulate TiO_2-filmed ultramicroelectrode. *Angew. Chem., Int. Ed.* **2018**, *57*, 3758–3762.